Comparison of theory and experiment for solute transport in highly heterogeneous porous medium

Fabrice Golfier, Michel Quintard, Fabien Cherblanc, Brendan Zinn, Brian Wood

Comparison of theory and experiment for solute transport in highly heterogeneous porous medium

Fabrice Golfier [a], Michel Quintard [b], Fabien Cherblanc [c], Brendan A. Zinn [d], Brian D. Wood [e,*]

[a] *Laboratoire Environnement, Géomécanique et Ouvrages – LAEGO – ENSG – INPL, Rue du Doyen Marcel Roubault, BP 40, 54501 Vandoeuvre-lès-Nancy, France*

[b] *Institut de Mécanique des Fluides (UMR CNRS 5502), Allée du Professeur Camille Soula, 31400 Toulouse, France*

[c] *Laboratoire de Mécanique et Génie Civil, Université Montpellier 2, Place Eugène Bataillon, 34000 Montpellier, France*

[d] *Ralph M. Parsons Laboratory, Department of Civil and Environmental Engineering, Massachusetts Institute of Technology, Cambridge, MA, United States*

[e] *Environmental Engineering, Oregon State University, Corvallis, OR 97331, United States*

In this work we compare the recently developed two-region mass transfer theory reported by Ahmadi et al. [A. Ahmadi, M. Quintard, S. Whitaker (1998), Transport in chemically and mechanically heterogeneous porous media, V, two-equation model for solute transport with adsorption, Adv. Water Resour. 1998;22:59–86] with experimental results reported by Zinn et al. [Zinn, B., L. C. Meigs, C. F. Harvey, R. Haggerty, W. J. Peplinski, C. F. Von Schwerin. Experimental visualization of solute transport and mass transfer processes in two-dimensional conductivity fields with connected regions of high conductivity. Environ Sci Technol 2004;38:3916–3926]. We find that the constant mass transfer coefficient predicted by the steady-state closure to the theory, when used with the macroscale transport equation, provides a reasonable prediction of the observed breakthrough curve. However, the use of a constant mass transfer coefficient does not allow good representation of the tailing that is observed in the data. We show that the mass transfer coefficient can be represented in terms of the eigenvalue expansion of a Green's function. For a steady solution to the closure problem, this expansion leads to the effective mass transfer coefficient being defined in terms of the harmonic average of the eigenvalues of the expansion; this is consistent with pre-vious work on this topic. To further investigate the influence of using a single, constant value for the mass transfer coefficient, we examine the solution to the mass transfer problem in terms of a mixed model, where the eigenvalues of one region (the inclusions) are kept, while the second region (the matrix) is treated as a homogenized material. The results from this comparison indicate that the mass transfer coefficient predicted via volume averaging using a quasi-steady closure could potentially be improved upon by development of new methods that retain more of the eigenvalues of the system.

Keywords: Mass transfer; Upscaling; Volume averaging; Mobile–immobile; Solute transport

1. Introduction

Although methods for treating solute transport in heterogeneous media with a low variance of the log-conductivity are now well established, corresponding methods for media with a high-variance of the log-conductivity (for which we will use the terminology *highly heterogeneous*) have only recently been explored in detail. One of the distinguishing features of solute transport in highly heterogeneous fields is that the transport behavior is often distinctly non-Fickian; that is, a conventional dispersive flux term in the conservation of mass equation does not capture all of the important solute transport behavior. Transport in highly heterogeneous fields is often observed experimentally by tailing in the spatial concentration field or solute

* Corresponding author. Fax: +1 541 737 3099.
E-mail address: brian.wood@oregonstate.edu (B.D. Wood).

Nomenclature

Roman Letters

a radius of a spherical or cylindrical inclusion (m)

$A_{\eta\omega}$ interfacial area of the interface between the matrix and inclusion material in an averaging volume or unit cell (m^2)

$A_{\eta,\text{effluent}}$ the area of the effluent boundary for the experimental flow cell (m^2)

$A_{\eta e}$ the area associated with the boundaries of the system volume (the flowcell boundaries in the case of the experimental work) (m^2)

a_v $=A_{\eta\omega}/\mathcal{V}$, area per unit volume of the solid–fluid interface (1/m)

$\mathbf{b}_{\eta\eta}$ closure variable that relates $\tilde{c}_\eta$ to sources involving $\nabla\langle c_\eta\rangle^\eta$; defined by Eq. (B.1) (m)

$\mathbf{b}_{\omega\omega}$ closure variable that relates $\tilde{c}_\omega$ to sources involving $\nabla\langle c_\omega\rangle^\omega$; defined by Eq. (B.2) (m)

$\mathbf{b}_{\eta\omega}$ closure variable that relates $\tilde{c}_\eta$ to sources involving $\nabla\langle c_\omega\rangle^\omega$; defined by Eq. (B.1) (m)

$\mathbf{b}_{\omega\eta}$ closure variable that relates $\tilde{c}_\omega$ to sources involving $\nabla\langle c_\eta\rangle^\eta$; defined by Eq. (B.2) (m)

c_η Darcy scale (associated with volume $\mathcal{V}_d$ in Fig. 1) concentration in the matrix (η-region) (kg/m^3)

c_ω Darcy scale concentration (associated with volume V_d in Fig. 1) in the inclusions (ω-region) (kg/m^3)

$\langle c_\eta\rangle$ superficial average concentration, as given by Eq. (34) (kg/m^3)

$\langle c_\eta\rangle^\eta$ intrinsic average concentration, as given by Eq. (34) (kg/m^3)

$\langle c_\omega\rangle$ superficial average concentration, as given by Eq. (35) (kg/m^3)

$\langle c_\omega\rangle^\omega$ intrinsic average concentration, as given by Eq. (35) (kg/m^3)

$\tilde{c}_\eta$ $=c_\eta-\langle c_\eta\rangle^\eta$, Darcy scale deviation concentration in the matrix (η-region) (kg/m^3)

$\tilde{c}_\omega$ $=c_\omega-\langle c_\omega\rangle^\omega$, Darcy scale deviation concentration in the inclusions (ω-region) (kg/m^3)

$c_{\eta,\text{effluent}}$ flux-averaged concentration across the flowcell effluent surface (kg/m^3)

c_0 initial concentration in the flowcell (kg/m^3)

c'_η deviation between $c_{\eta,\text{effluent}}$ and $\langle c_\eta\rangle^\eta$, defined by Eq. (65) ($kg/m^3$)

$C_{\eta\omega}$ $=\langle c_\eta\rangle^\eta-\langle c_\omega\rangle^\omega$, as defined in Appendix C (kg/m^3)

D_{mol} the (dilute solution) molecular diffusion coefficient for the solute in water (m^2/s)

$D_{\text{eff},\eta}$ Darcy scale (associated with volume $\mathcal{V}_d$ in Fig. 1) effective diffusion coefficient for solute in the matrix (η-region) (m^2/s)

$D_{\text{eff},\omega}$ Darcy scale (associated with volume $\mathcal{V}_d$ in Fig. 1) effective diffusion coefficient for solute in the inclusions (ω-region) (m^2/s)

$\mathbf{D}^*_\eta$ Darcy scale (associated with volume $\mathcal{V}_d$ in Fig. 1) total dispersion tensor for the matrix (η-region) (m^2/s)

$\mathbf{D}^*_\omega$ Darcy scale (associated with volume $\mathcal{V}_d$ in Fig. 1) total dispersion tensor for the inclusions (ω-region) (m^2/s)

$\mathbf{D}^*_{\eta\eta}$ Macroscale (associated with volume $\mathcal{V}$ in Fig. 1) effective dispersion tensor for the matrix (η- region) (m^2/s)

$\mathbf{D}^*_{\omega\omega}$ Macroscale (associated with volume $\mathcal{V}$ in Fig. 1) effective dispersion tensor for the matrix (η-region) (m^2/s)

$\mathbf{D}^*_{\eta\eta,mixed}$ Macroscale effective dispersion tensor for the matrix (η-region) as defined for the mixed model (m^2/s)

K_η Darcy-scale hydraulic conductivity for the matrix (η-region) (m/s)

K_ω Darcy-scale hydraulic conductivity for the inclusions (ω-region) (m/s)

ℓ_η, ℓ_ω characteristic lengths associated with the Darcy scale (see Fig. 1, Level II) (m)

L characteristic length associated with the macroscale (see Fig. 1, Level III) (m)

ℓ_i lattice vector for the ith direction ($i=1,2,3$) (m)

$\mathbf{n}_{\eta\omega}$ $=-\mathbf{n}_{\omega\eta}$, unit normal vector, pointing from the η phase toward the ω phase (−)

$\mathbf{n}_{\eta e}$ unit normal vector, pointing outward from the η phase toward the outside of the system volume (or flowcell boundaries for the case of the experimental work) (−)

$\mathbf{n}_{\text{exit}}$ unit normal vector, pointing outward from the flowcell effluent surface (−)

$Pe_{\omega\omega}$ $=\langle v_\omega\rangle^\omega a^2/LD_{\text{eff},\omega}$, a macroscale Péclet number for the inclusions (−)

$Pe_{\eta\eta}$ $=\langle v_\eta\rangle^\eta L/D_{\text{eff},\eta}$, a macroscale Péclet number for the matrix (−)

$Pe_{\eta\omega}$ $=\langle v_\eta\rangle^\eta a/D_{\text{eff},\omega}$, a mixed macroscale Péclet number (−)

Q generic flow rate (m^3/s)

Q_{High} the high flow rate for the flowcell experiments (1.32 mL/min) (mL/min)

Q_{Low} the low flow rate for the flowcell experiments (0.66 mL/min) (mL/min)

R_0 characteristic length associated with a macroscale averaging volume (Level II of Fig. 1) (m)

r_η closure variable that relates $\tilde{c}_\eta$ to $(\langle c_\eta\rangle^\eta-\langle c_\omega\rangle^\omega)$; defined by Eq. (B.1) (−)

r_ω closure variable that relates $\tilde{c}_\omega$ to $(\langle c_\eta\rangle^\eta-\langle c_\omega\rangle^\omega)$; defined by Eq. (B.2); also interpretable as the first integral of a Green's function as indicated by Eq. (C.23) (−)

t_η, t_ω characteristic times associated with Darcy scale concentration changes in the matrix and inclusions, respectively (s)

T^*_η characteristic times associated with macroscale concentration changes in the matrix (s)

$\mathbf{v}_\eta$ Darcy scale fluid velocity vector for the matrix (m/s)

$\mathbf{v}_\omega$ Darcy scale fluid velocity vector for the inclusions (m/s)

$\langle \mathbf{v}_\eta \rangle^\eta$ intrinsic average macroscale fluid velocity vector for the matrix (m/s)

$\langle \mathbf{v}_\omega \rangle^\omega$ intrinsic average macroscale fluid velocity vector for the inclusions (m/s)

$\tilde{\mathbf{v}}_\eta$ $=\mathbf{v}_\eta - \langle \mathbf{v}_\eta \rangle^\eta$, fluid velocity deviation vector for the matrix (m/s)

$\tilde{\mathbf{v}}_\omega$ $=\mathbf{v}_\omega - \langle \mathbf{v}_\omega \rangle^\omega$, fluid velocity deviation vector for the inclusions (m/s)

$\mathbf{v}_{\eta,\text{effluent}}$ velocity normal to the flowcell outlet surface of the experimental flow cell (m/s)

$\mathscr{V}$ volume associated with a macroscale averaging volume, as defined in Fig. 1 (m^3)

$\mathscr{V}_d$ volume associated with a Darcy scale averaging volume, as defined in Fig. 1 (m^3)

V_η volume associated with the matrix within an averaging volume (m^3)

V_ω volume associated with the inclusions within an averaging volume (m^3)

$V_{\beta,\eta}$, $V_{\beta,\omega}$ volume fraction of fluid within the matrix and inclusions, respectively (see Appendix A) (m^3)

Greek Letters

α^* effective mass transfer coefficient (1/s)

$\alpha_{L,\eta}$,$\alpha_{L,\omega}$ Darcy-scale longitudinal dispersivity for the matrix and inclusions, respectively (m)

$\alpha_{T,\eta}$, $\alpha_{T,\omega}$ Darcy-scale transverse dispersivity for the matrix and inclusions, respectively (m)

δ_{ij} Kronecker delta symbol

η phase indicator for the matrix (−)

ω phase indicator for the inclusions (−)

κ $=K_\eta/K_\omega$, ratio of hydraulic conductivities of the matrix to that of the inclusions (−)

σ^2_Y variance of the log-transformed hydraulic conductivity field (−)

Ω_η, Ω_ω non-conventional terms in the macroscale mass balance equations, as defined by Eqs. (B.42) and (B.43), respectively

breakthrough curves (e.g. [1–6]). A large variety of methods have begun to be explored for describing transport in such systems, including fractional derivative formulations [2–4], continuous time random walks [5,6], convolution integro-differential equation approaches [7,8], cumulant expansion/renormalization methods [9–16], homogenization theory [17,18], and volume averaging [19].

First-order mass transfer models (also known as linear driving force models) are the most widely applied methods for representing mass transfer and transport in media with regions of distinctly different hydraulic conductivity. Generalizations of the approach have considered systems in which the spatial hydraulic conductivity field is partitioned into a sequence of discrete conductivities [20–24]. The advantage of this approach is that the overall variability in hydraulic conductivity is maintained, but the overall effect of the heterogeneities can be studied by examining the interaction of a finite number of non-overlapping spatial fields each with reasonably small variance in the log hydraulic conductivity.

In the simplest case, the spatial conductivity field is binary, and an example of such a field appears in Fig. 1, Level II. In Fig. 1, the binary field is represented as a high-conductivity matrix material (labeled as the η-region, with hydraulic conductivity K_η) with low-conductivity inclusions (labeled as the ω-region, with hydraulic conductivity K_ω). Such structures are common in the subsurface [25,26], so binary media represent a useful starting point for many studies of the heterogeneous subsurface. In this work, the length scale r_0 illustrated in Fig. 1, Level III will be termed the *Darcy* or *microscale*; the volume associated with this scale is smaller than the volume of the inclusions, but sufficiently large such it provides a continuous representation of the porous medium. The length scale R_0 illustrated in Fig. 1, Level II will be termed the *macroscale*, and the volume associated with this scale is larger than an individual inclusion, but smaller than the entire system of interest.

First-order mass transfer models are usually applied with a constant effective mass transfer coefficient (e.g. [27–35]). It has been pointed out by a number of researchers that the use of a constant mass transfer coefficient is applicable only under certain limiting conditions [28,36]. Parker and Valocchi [28] have generated specific time-scale constraints for the validity of the first-order mass transfer model. Others have pointed out that the effective mass transfer depends not only upon the media properties, but on the initial and boundary conditions as well [36,37], suggesting that the general construction of a linear mass transfer model would be done most appropriately in a non-local context. In response to these shortcomings, several non-local models have been developed for the linear mass transfer model, and this includes the diffusion into spherical grains models [22,37], and the multi-rate mass transfer models [3,38,39].

The first-order mass transfer models described above have been developed either heuristically or by a geometry-specific analysis. Recently, the development of a first-order mass-transfer model has been investigated for more general conditions using the method of volume averaging (e.g. see the studies by Ahmadi et al. [20] and Cherblanc et al. [40,41]). These developments have provided schemes in which the effective linear mass transfer coefficient can be determined for an inclusion geometry that may be non-spherical, and they have provided specific constraints for assessing the range of validity of the method. Both the asymptotic [20,40,41] and transient-non-local approaches have been developed in this context [42,43].

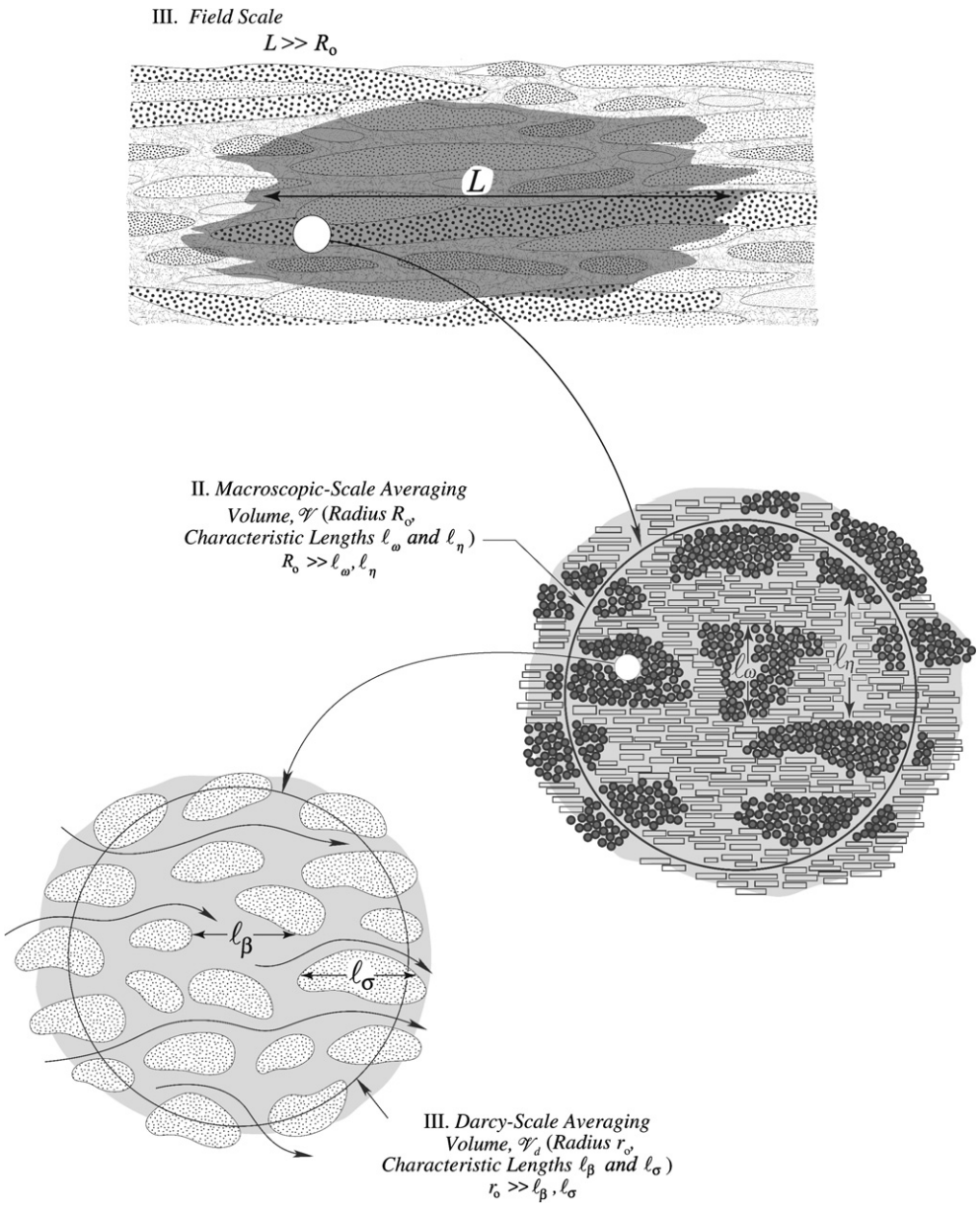

Fig. 1. Hierarchy of scales associated with a highly heterogeneous binary porous medium.

For our analysis the macroscale transport equations are a simplified version of that reported by Ahmadi et al. [20], and they take the classical form for a two-region model:

Matrix (η-*region*):

$$\underbrace{\frac{\partial\langle c_\eta\rangle^\eta}{\partial t}}_{\text{Accumulation}} = \underbrace{\nabla\cdot[\mathbf{D}^*_{\eta\eta}\cdot\nabla\langle c_\eta\rangle^\eta]}_{\text{Dispersion}} - \underbrace{\langle\mathbf{v}_\eta\rangle^\eta\cdot\nabla\langle c_\eta\rangle^\eta}_{\text{Convection}} - \underbrace{\varepsilon_\eta^{-1}\varphi_\eta^{-1}\alpha^*(\langle c_\eta\rangle^\eta - \langle c_\omega\rangle^\omega)}_{\text{Inter-phase mass transfer}} \quad (1)$$

Inclusion (ω-*region*):

$$\underbrace{\frac{\partial\langle c_\omega\rangle^\omega}{\partial t}}_{\text{Accumulation}} = \underbrace{\nabla\cdot[\mathbf{D}^*_{\omega\omega}\cdot\nabla\langle c_\omega\rangle^\omega]}_{\text{Dispersion}} - \underbrace{\langle\mathbf{v}_\omega\rangle^\omega\cdot\nabla\langle c_\omega\rangle^\omega}_{\text{Convection}} + \underbrace{\varepsilon_\omega^{-1}\varphi_\omega^{-1}\alpha^*(\langle c_\eta\rangle^\eta - \langle c_\omega\rangle^\omega)}_{\text{Inter-phase mass transfer}} \quad (2)$$

In these equations, additional terms (dispersive cross-terms and convective term corrections [20,40]), have been discarded compared to the original generalized model. These were found to make a negligible contribution in the test cases under investigation in this paper.

The purpose of this work is to compare theory and experiment for two-region systems where significant mass transfer effects are present. We examine two different theoretical approaches as follows: (1) a linear first-order method where the mass transfer process is represented by an effective mass transfer model, and (2) a mixed method in which the inter-phase mass transfer process is represented by a Fickian diffusive flux. Both approaches are developed using a volume averaging. The specific goals of this work are (1) to assess the relative merits and drawbacks of these two approaches, (2) to assess the ability of each method to

predict the breakthrough curves for the experimental systems analyzed, and (3) to make recommendations for model use and directions for additional theory development.

The remainder of the paper is organized as follows: in Section 2 we briefly describe the two-region experimental flowcell systems of Zinn et al. [44], which provided the breakthrough curves used in the subsequent analysis. In Section 3 we describe the two-equation models (the first-order mass transfer and mixed models) developed using volume averaging method. In Section 4, we present the numerical methods used for the computation of the effective properties and for the mixed model; results for the two models are presented. Finally, in Section 5 we provide some discussions of the results, and in Section 6 we offer some conclusions.

2. Laboratory experiments and parameter estimates

In this section we briefly outline the operational and physical set up of the two-region flowcell experiments. Although the physical properties of the porous media used in these experiments were measured independently, the properties of the media when packed in a particular flowcell system vary somewhat from the independently measured values. These deviations result primarily from the packing effort itself; what is actually realized within the flowcell is different from the independently measured values because of (uncontrollable) differences in the microstructure of the media during packing. Because of these differences, a calibration and validation step was also included as part of the experimental methods. The purpose of this step was to use a fully-resolved Darcy-scale model of the experimental system to compare the predicted breakthrough curves with those observed. Small modifications of the physical parameters (within the range of values expected for each medium) could then be introduced to improve the estimates of the physical parameters as actually realized in the experimental system.

Table 1
Simulation data for the high and intermediate conductivity contrast media

Parameter	High contrast, $\kappa = 1800$	Low contrast, $\kappa = 300$
$D_{\mathrm{eff},\eta}$, m^2/s	5.7×10^{-10}	5.7×10^{-10}
$D_{\mathrm{eff},\omega}$, m^2/s	5.7×10^{-10}	5.7×10^{-10}
ε_η	0.505	0.505
ε_ω	0.505	0.505
$\alpha_{\mathrm{L},\eta}$, m	0.004	0.002
$\alpha_{\mathrm{T},\eta}$, m	0.004	0.002
$\alpha_{\mathrm{L},\omega}$, m	0.0004	0.0002
$\alpha_{\mathrm{T},\omega}$, m	0.0004	0.0002
Q_{High}, cm^3/min	0.66	0.63
Q_{Low}, cm^3/min	1.32	1.26
σ_Y^2	12.4	7.2

2.1. Experiment process parameters

In this paper we examine two of the three experimental systems studied by Zinn et al. [44]. These correspond to (1) the *intermediate* contrast in hydraulic conductivity (experiments 2a and 2b) and (2) the *high* contrast in hydraulic conductivity (experiments 3a and 3b). The physical parameters for these two experimental systems are presented in Table 1, and the two Péclet numbers for these experiments are plotted in Fig. 2. The experiments were conducted under

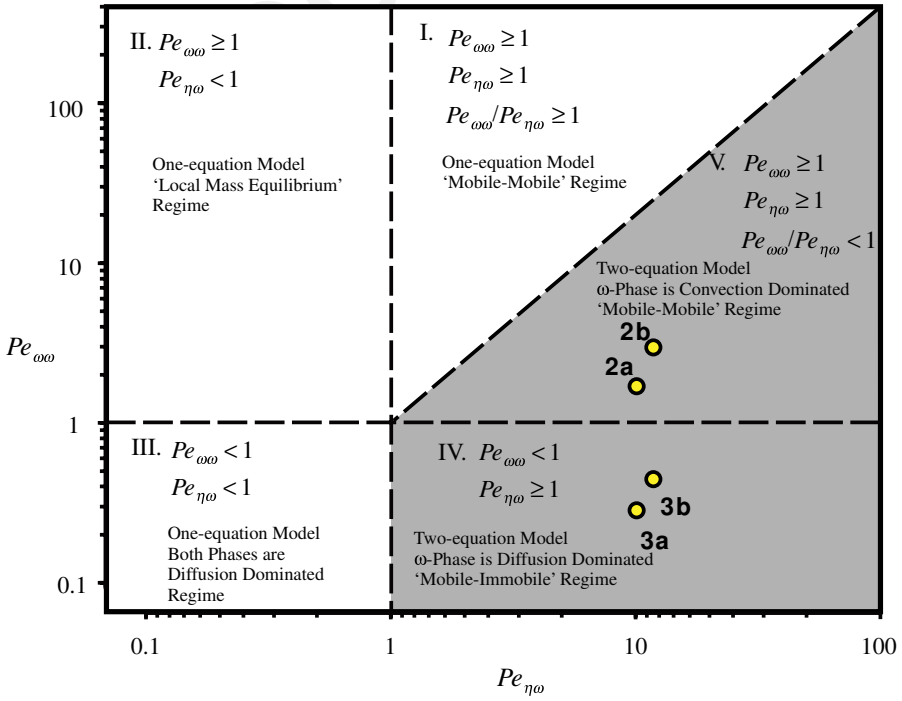

Fig. 2. Plot illustrating the empirically-classified transport regimes as a function of the two Péclet numbers, $Pe_{\omega\omega}$ and $Pe_{\eta\omega}$. The point correspond to experiments conducted by Zinn et al. [44]. Experimental conditions were as follows: Experiment 2a: $\kappa = 300$, $Q = 0.66$ mL/min. Experiment 2b: $\kappa = 300$, $Q = 1.32$ mL/min. Experiment 3a: $\kappa = 1800$, $Q = 0.66$ mL/min. Experiment 3b: $\kappa = 1800$, $Q = 1.32$ mL/min (diagram adapted from Zinn et al. [44]).

conditions that correspond to a 'mobile–mobile' (e.g. [45–50]) regime for experiments 2a and 2b, and a mobile–immobile (e.g. [27,48,51–54]) regime for experiments 3a and 3b. We specifically do not consider the *low* contrast case from Zinn et al. [44] because our focus is specifically on systems where the variance of the log-K distribution is greater than 1. The geometry of the experimental system used for these experiments is illustrated in Fig. 3.

Zinn et al. [44] developed a useful empirical categorization of possible transport regimes for such binary systems, and a slightly modified version of that plot is presented here as Fig. 2. For this classification, two Péclet numbers, measuring the relative importance of convection to diffusion, appear. These are defined by

$$Pe_{\omega\omega} = \frac{\langle v_\omega \rangle^\omega a}{D_{eff,\omega}} \tag{3}$$

$$Pe_{\eta\omega} = \frac{\langle v_\eta \rangle^\eta a}{D_{eff,\omega}} \left(\frac{a}{L}\right) \tag{4}$$

Here, a represents the characteristic length (radius) of the inclusions, L is the characteristic length of the matrix material (observation scale), $\langle v_\eta \rangle^\eta$ is the average pore-water velocity in the inclusions, $\langle v_\omega \rangle^\omega$ is the average pore-water velocity of the matrix material, and $D_{\mathrm{eff},\omega}$ is the effective diffusion coefficient in the inclusions. The first of these two Péclet numbers represents the ratio of convective to diffusive fluxes in the inclusions (or, equivalently, the ratio of the characteristic time for diffusion in the inclusions divided by the characteristic time for advection across the inclusions). The second to these two groupings is a mixed region Péclet number, representing the ratio of the convective flux in the matrix to the diffusive flux in the inclusion (or, equivalently, the ratio of the characteristic time for diffusion in the inclusions divided by the characteristic time for convection across the observation region in the matrix material). Note that in the Zinn et al. [44] work the second of these two dimensionless groupings was expressed as a Damköhler number (Da), where $Pe_{\eta\omega} = Da^{-1}$. There is a third Péclet number that one can define for the matrix material by

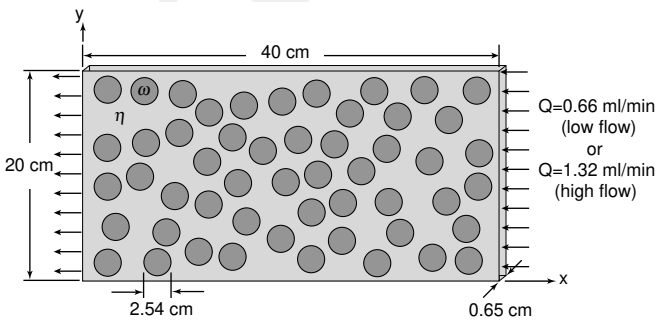

Fig. 3. Geometry of the experimental system used for the transport experiments of Zinn et al. [44]. Inclusions are represented as dark gray (low-conductivity); the high-conductivity background material is represented by light grey.

$$Pe_{\eta\eta} = \frac{\langle v_\eta \rangle^\eta L}{D_{\mathrm{eff},\eta}} = Pe_{\eta\omega}\left[\frac{L^2}{a^2}\frac{D_{\mathrm{eff},\omega}}{D_{\mathrm{eff},\eta}}\right] \tag{5}$$

It has been implicitly assumed in the work of Zinn et al. [44] that the term in the bracket is of order unity, so that $Pe_{\eta\eta} = \mathrm{O}(Pe_{\eta\omega})$. Note that this is not a restriction for the theoretical developments reported here, this approximation applied only to the results reported by Zinn et al. [44].

Previous results obtained by Parker and Valocchi [28] indicate that a first-order mass transfer model should be valid under the constraint:

$$\frac{2(1-\beta)}{175} Pe_{\eta\omega}^2 < 0.25 \tag{6}$$

Note that in this expression, our definition of $Pe_{\eta\omega}$ is equivalent to the parameter γ^{-1} in [28], and $\beta = \varepsilon_\eta \varphi_\eta / (\varepsilon_\omega \varphi_\omega + \varepsilon_\eta \varphi_\eta)$. Here we have assumed that the observation point is the column effluent, and that the retardation factor is identically equal to 1. Solving this for the Péclet number, this constraint can be expressed

$$Pe_{\eta\omega} < \left(\frac{175}{8(1-\beta)}\right)^{\frac{1}{2}} \tag{7}$$

From the parameters in Table 1, we find that for the experimental systems reported by Zinn et al. [44], this constraint suggests that $Pe_{\eta\omega}$ should be less than about 10. From Fig. 2, it is apparent that these two sets of experiments are very near the boundary where the one-equation linear transport model is valid.

2.2. Flowcell geometry and operation

A flowcell system with inclusions of contrasting conductivity was created by packing a 40 cm wide by 20 cm high by 0.65 cm thick chamber with low-conductivity circular emplacements of 2.54 cm diameter and supporting high-conductivity background media. Fifty-three inclusions were placed in the chamber in a computer-generated random pattern, with the inclusions being no closer to each other than 6 mm and no closer to the edges of the chamber than 4 mm. The inclusions constituted 33.5% of the tank volume. The geometry of the system has been presented in Fig. 3.

The conductivity of the matrix material was on the order of 10^{-4} m/s (grain size average of 2 mm diameter), and the conductivity of the inclusions was a factor of 1800 or 300 lower depending upon the experiment. The average grain sizes of the porous media used to construct the inclusions was 57 μm and 135 μm diameter, respectively. Both materials had a measured porosity between 0.425 ± 0.025; however, because the flow cell was very thin compared to the grain size (particularly for the matrix material) the porosity in place may have been much higher due to packing non-uniformities. Numerical simulations of the flowcells (described in Section 4) suggested that the porosity in the matrix material might be as high as

$\varepsilon_\eta = 0.505$, and this value was assumed for the remainder of this study.

Flow conditions at the inlet and outlet were controlled by carefully-designed manifolds and screens. Water was pumped into the chamber using a computer-controlled ISCO model 500 D syringe pump. The flowcell was flushed with CO_2 gas and then de-aired water to allow saturation without creating trapped air. Transport experiments were conducted by first saturating the flowcell with a solution of a dye tracer (FD&C Blue Number 1) at a concentration of 30 mg/L. The transport experiments were conducted in a 'flushing' mode, where clean water replaced the dye filling the flowcell. For each contrast in hydraulic conductivity, two transport experiments were conducted with flowrates of 0.66 mL/min and 1.32 mL/min.

2.3. Concentration measurement

Spatial distributions of the dye concentration were imaged by using a 60 MHz fluorescent light source with a neutral density filter to provide uniform backlighting. The system was fan-cooled to prevent heating of the chamber. A 14-bit liquid-cooled CCD (charge-coupled device) camera captured a sequence of images at specified time intervals. A combination of filters was used on the camera to create a 600–700 nm band pass filter for optimal light absorbance. Data were recorded in terms of pixel intensities (0–4095). Each pixel resolved an area of the chamber approximately 400×400 μm. Outflow dye concentration was measured with a spectrophotometer (Varian). The tracer, FD&C Blue Number 1, possesses a distinct absorbance peak with strong linearity. The photometer was computer-controlled and programmed to target the 630 nm and 409 nm wavelengths of FD&C Blue Number 1. The 630 nm peak was effective at measuring concentrations from 0.01 mg/L to approximately 20 mg/L. The 409 nm peak was effective from 0.1 mg/L to well above the maximum concentration of 30 mg/L. Outflow concentrations were calculated from spectrophotometer measurements at both wavelengths. A cutoff concentration value where both measurements agreed with each other was chosen (near 10 mg/L). Concentrations calculated using the 409 nm calibration curve were employed above the cutoff value, while the 630 nm calibration was used below this cutoff value. This method did not introduce discontinuities in the data because of the strong agreement between the two different estimates within this overlap range.

2.4. Validation and calibration of the Darcy-scale physical properties

In the original work reporting the results of the flowcell data sets, Zinn et al. [44] did not validate their dataset with a Darcy scale model of the system in which the inclusions were fully resolved. The utility of such a model is that it would allow for a more precise validation/calibration of the experimental parameters involved, in particular the values of the porosity and dispersion coefficient for each region in the experimental systems. The exact values for these parameters were known only for the individual media comprising the matrix and inclusion materials. As described above the actual properties of the materials used to construct the porous medium would be expected to be slightly different from the independently measured values due to changes induced by packing of the media within the cell.

For the work reported here, a Darcy-scale model was developed to directly simulate the intermediate- and high-contrast experimental systems reported by Zinn et al. [44]. The set of balance equations used to model the system at the Darcy scale were as follows [55]:

Darcy scale transport equations:

$$\varepsilon_\eta \frac{\partial c_\eta}{\partial t} + \nabla \cdot (\varepsilon_\eta \mathbf{v}_\eta c_\eta) = \nabla \cdot [\varepsilon_\eta \mathbf{D}^*_\eta \cdot \nabla c_\eta] \quad \text{in the } \eta\text{-region} \tag{8}$$

$$c_\eta = c_\omega \quad \text{at } A_{\eta\omega} \tag{9}$$

$$-\mathbf{n}_{\eta\omega} \cdot (\varepsilon_\eta \mathbf{v}_\eta c_\eta - \varepsilon_\eta \mathbf{D}^*_\eta \cdot \nabla c_\eta) = -\mathbf{n}_{\eta\omega} \cdot (\varepsilon_\omega \mathbf{v}_\omega c_\omega - \varepsilon_\omega \mathbf{D}^*_\omega \cdot \nabla c_\omega), \quad \text{at } A_{\eta\omega} \tag{10}$$

$$\varepsilon_\omega \frac{\partial c_\omega}{\partial t} + \nabla \cdot (\varepsilon_\omega \mathbf{v}_\omega c_\omega) = \nabla \cdot [\varepsilon_\omega \mathbf{D}^*_\omega \cdot \nabla c_\omega] \quad \text{in the } \omega\text{-region} \tag{11}$$

$$c_\eta = 0 \quad \text{at inlet}, -\mathbf{n}_{\eta e} \cdot \varepsilon_\eta \mathbf{D}^*_\eta \cdot \nabla c_\eta = 0 \quad \text{at outlet}, \quad -\mathbf{n}_{\eta e} \cdot (\varepsilon_\eta \mathbf{v}_\eta c_\eta - \varepsilon_\eta \mathbf{D}^*_\eta \cdot \nabla c_\eta) = 0 \quad \text{at all other boundaries} \tag{12}$$

$$c_\eta = c_0 \quad \text{in the } \eta\text{-region at } t = 0 \tag{13}$$

$$c_\omega = c_0 \quad \text{in the } \omega\text{-region at } t = 0 \tag{14}$$

Darcy scale steady flow equations:

$$\nabla \cdot (\varepsilon_\eta \mathbf{v}_\eta) = 0 \quad \text{in the } \eta\text{-region} \tag{15}$$

$$\nabla \cdot (\varepsilon_\omega \mathbf{v}_\omega) = 0, \quad \text{in the } \omega\text{-region} \tag{16}$$

$$\mathbf{v}_\eta = -\frac{K_\eta}{\varepsilon_\eta} \nabla h_\eta, \quad \mathbf{v}_\omega = -\frac{K_\omega}{\varepsilon_\omega} \nabla h_\omega \tag{17}$$

$$\mathbf{v}_\eta = \mathbf{v}_\omega, \quad \text{at } A_{\eta\omega} \tag{18}$$

$$h_\eta = h_0 \quad \text{at inlet}, \quad h_\eta = h_1 \quad \text{at outlet}, \quad \mathbf{n}_{\eta e} \cdot \mathbf{v}_\eta = 0 \quad \text{at all other boundaries} \tag{19}$$

In Eqs. (8)–(19), c_η and c_ω are the intrinsic average concentrations in the η- and ω-regions respectively, ε_η and ε_ω are the porosities, $\mathbf{v}_\eta$ and $\mathbf{v}_\omega$ are the intrinsic average pore velocities, $\mathbf{D}^*_\eta$ and $\mathbf{D}^*_\omega$ are the total dispersion tensors (diffusion plus hydrodynamic dispersion) for the two regions (cf. Whitaker [56, Chapter 3]; Bear [57, Section 7-3]), K_η and K_ω are the hydraulic conductivities for the two regions, and h_η and h_ω are the corresponding hydraulic heads. The interfacial area between the two regions is denoted by $A_{\eta\omega}$, and the outward pointing normal vector for the volume boundaries of the cell is given by $\mathbf{n}_{\eta e}$. The porosity of intrinsic average Darcy concentration and pore velocity can be defined explicitly in terms of the pore-scale variables by the following

$$\varepsilon_\eta = \frac{V_{\text{fluid}}}{\mathscr{V}_d} = \frac{V_\beta}{\mathscr{V}_d} \quad \text{in the } \eta\text{-region} \tag{20}$$

$$\varepsilon_\omega = \frac{V_{fluid}}{\mathscr{V}_d} = \frac{V_\beta}{\mathscr{V}_d} \quad \text{in the } \omega\text{-region} \tag{21}$$

The parameters used for these computations are listed in Table 1. Note that for these computations, we have adopted the notation

$$\kappa = K_\eta / K_\omega \tag{22}$$

where K_η and K_ω represent the hydraulic conductivity in the matrix and inclusions, respectively.

A multiple-step numerical method was adopted. In this approach the transport equation is split into a hyperbolic part (convective terms) and an elliptic part (diffusive term). A second-order TVD-scheme proposed by Takacs [58] was used for the hyperbolic part in order to reduce numerical diffusion [59], whereas the dispersive part is solved using a implicit discretization based on a nine-point scheme [60]. A uniform mesh (400 in x by 200 in y) was used for simulations. The Darcy-scale hydrodynamic dispersion tensor (note that this is the scale associated with Eqs. (27)–(33)) was defined by [57,61]

$$D^*_{ij,\eta} = (\alpha_{\text{L},\eta} - \alpha_{\text{T},\eta}) \frac{v_{i,\eta} v_{j,\eta}}{|\mathbf{v}_\eta|} + \alpha_{\text{T},\eta} |\mathbf{v}_\eta| \delta_{ij} + D_{\text{eff},ij,\eta} \delta_{ij} \tag{23}$$

$$D^*_{ij,\omega} = (\alpha_{\text{L},\omega} - \alpha_{\text{T},\omega}) \frac{v_{i,\omega} v_{j,\omega}}{|\mathbf{v}_\omega|} + \alpha_{\text{T},\omega} |\mathbf{v}_\omega| \delta_{ij} + D_{\text{eff},ij,\omega} \delta_{ij} \tag{24}$$

Here, α_{L} and α_{T} are the longitudinal and transverse local dispersivities, $\mathbf{v}$ is the local (Darcy-scale) velocity vector and $D_{\text{eff},ij,\eta}$ is the local-scale effective diffusion tensor, and δ_{ij} is the Kronecker delta function (NB, Bear [57] uses the notation $\boldsymbol{D}_h$ for this tensor). The molecular diffusion coefficient of the tracer in water was reported by Zinn et al. [44] as $D_{\text{mol}} = 5.7 \times 10^{-10}\ \text{m}^2\ \text{s}^{-1}$. The longitudinal dispersivity for the high conductivity media was reported to be 0.00625 ± 0.0013 m, and for the low conductivity material, the longitudinal dispersivity was reported to be 0.0022 ± 0.0003 m [B. Zinn, personal communication]. These estimates were from a sequence of laboratory measurements on the porous media itself, but the exact value of the dispersivity as packed for any one experiment was not measured.

In our direct Darcy-scale simulations of the experimental data, we varied the porosities, dispersivities, and flow rates from the reported estimated values in order to optimize the simulation of the observed data. The primary reason that the reported parameters were not treated as exact is that the original publication [44] reported these parameters either as estimates or with significant uncertainties associated with them. By allowing small variations in ε_η, ε_ω, $\alpha_{\text{L},\eta}$, $\alpha_{\text{L},\omega}$, and Q value we were able to develop a set of parameters that was both reasonable in light of the uncertainties associated with the experimental conditions, and also provided good representation of the experimental breakthrough curves. These adjustments were conducted manually, with no attempt to optimize the set of parameters by, for example, a least-squares scheme.

The values determined from the Darcy-scale simulation are reported on Table 1. Of the parameters varied, the porosity values in particular were the only ones that were significantly different from the values measured experimentally. Several possibilities might explain this discrepancy: (1) the method used to measure the porosity was only approximate [44], and did not account for the fences used to contain the medium used for the inclusions (there was an approximate 1–2% increase in porosity when including these); (2) according to the literature it is possible for FD&C Blue Number 1 adsorb to surfaces [62], and this would have been observed in our fitting of the data as a decrease in the effective velocity of the solute, which ultimately would be manifest by an increase in porosity.

In Fig. 4 we have plotted the solute breakthrough curves (effluent concentration as a function of time) for the high- and intermediate contrast cases under the low flow conditions ($Q = 0.66$ mL/min). These curves have been normalized by the initial concentration in the flow cells,

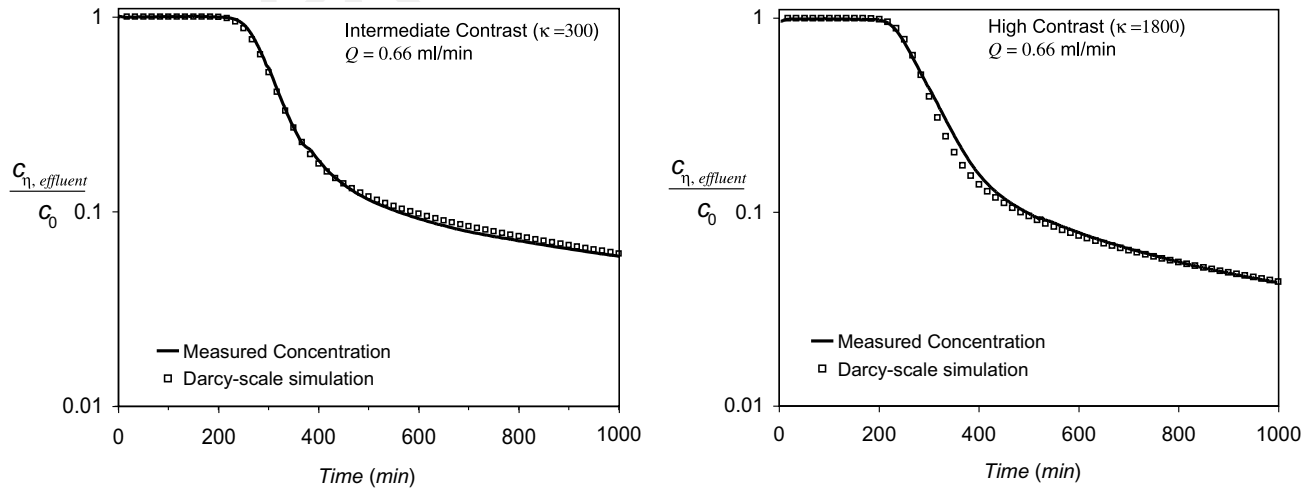

Fig. 4. Concentration breakthrough curves for the high- and intermediate-contrast flowcells. The results of the Darcy-scale validation simulations are shown as a solid line.

c_0; because our emphasis is on the behavior of the 'tails' of the breakthrough curves, we have also plotted the vertical axis on a logarithmic scale. Physically, the effluent solute concentration is flux-averaged over the area of the flowcell exit. We will denote the effluent solute concentration by $c_{\eta,\text{effluent}}$; it is defined by

$$c_{\eta,\text{effluent}} = \frac{1}{Q_{\eta,\text{effluent}}} \int_{A_{\eta,\text{effluent}}} \mathbf{n}_{\eta e} \cdot (\mathbf{v}_\eta c_\eta) \mathrm{d}A \tag{25}$$

where

$$Q_{\eta,\text{effluent}} = \int_{A_{\eta,\text{effluent}}} \mathbf{n}_{\eta e} \cdot \mathbf{v}_\eta \, \mathrm{d}A \tag{26}$$

Here $A_{\eta,\text{effluent}}$ represents the area of the flowcell exit, $\mathbf{n}_{\eta e}$ the outward-pointing unit normal vector for this surface. Because the flowcells were operated in 'flushing mode', the normalized effluent concentration starts at 1 and gradually decreases to 0 as solute-free water enters the flowcell. Similar results were obtained for the second flow rate. Reasonable agreement is obtained between the simulated and measured effluent concentrations, indicating at least that our estimates for the physical parameters are consistent with the observed data.

A comparison of the dimensionless concentration field obtained from the experimental system and from numerical simulations appears in Fig. 5. The two fields compare

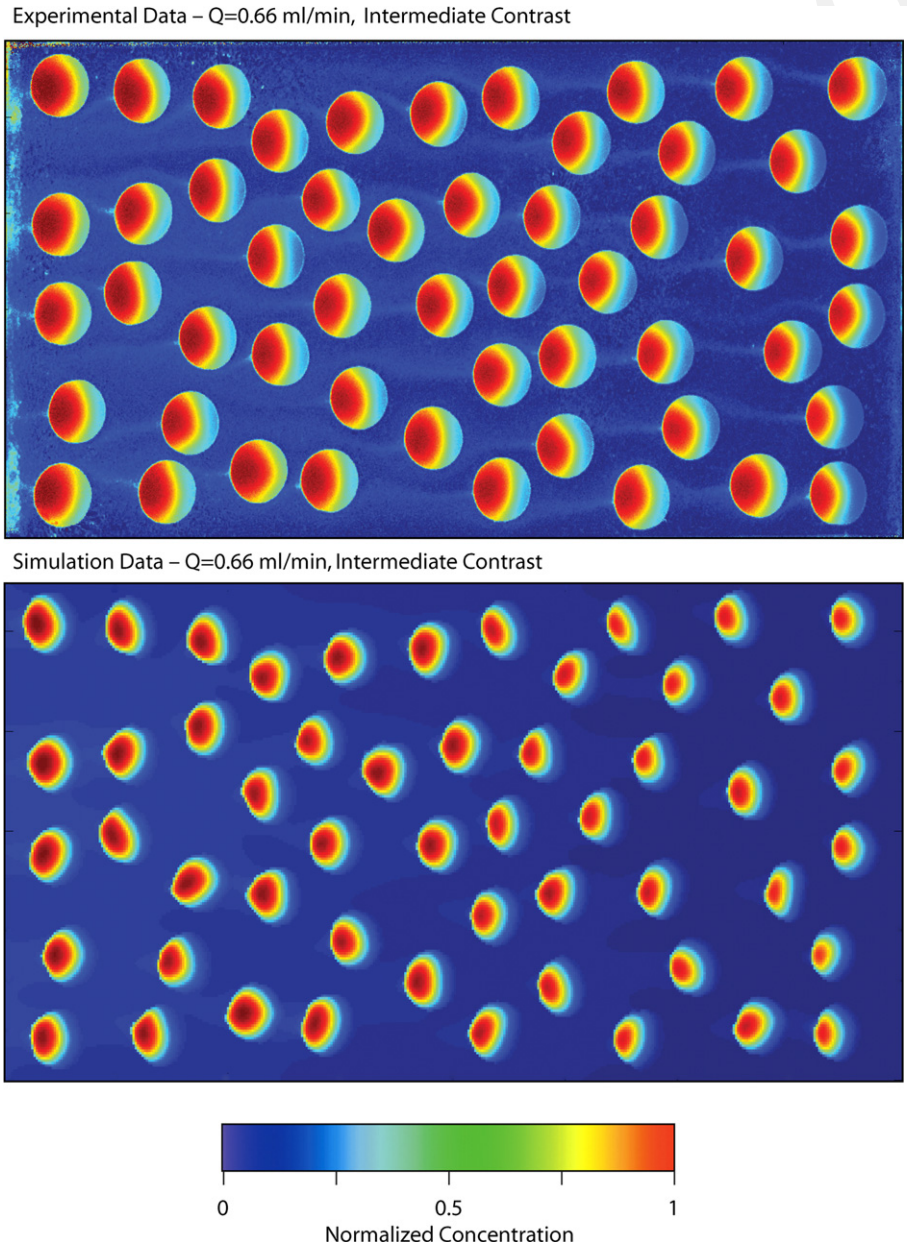

Fig. 5. Comparison of the dimensionless concentration field observed inside the chamber (top), and predicted from simulations (bottom). These fields are for the intermediate-contrast case with a flow rate of 0.66 mL/min at $t = 500$ min. The discrepancy between observations and numerical simulations are partly experimental artifact due to the filtering process.

reasonably well, with both fields showing the combination of diffusion and convection in the inclusions. Because of the optical filtering mechanisms that were used, the residual concentration in the inclusions observed for the experimental data at this time represent in part an experimental artifact.

The results above provide confirmation that the experimental system, as predicted by a Darcy-scale numerical model where no upscaling has been done, performs as it was intended to within the experimental uncertainties reported originally by Zinn et al. [44].

3. Two-equation models for mass transport

We present two different two-equation models for describing mass transport in highly heterogeneous media. The first is a linear mass transfer model with a constant coefficient, developed by volume averaging with a steady closure scheme. The second is a mixed model. This second model is similar to previously proposed spherical diffusion models [22,32,37], although because it does not rely explicitly on an eigenvalue expansion solution, it has no restriction associated with the particular geometries for which it can be applied.

3.1. Volume averaging with steady-state closure

The upscaling from the pore scale, characterized by the characteristic lengths ℓ_β and ℓ_σ, to the field scale, characterized by length scale L, takes place in two averaging steps for the hierarchical system illustrated in Fig. 1. The upscaling from the pore-scale to the Darcy scale (the averaging volume, $\mathscr{V}_d$, associated with Level I in Fig. 1) has been completed previously [55]. The second level of upscaling from the Darcy to the field scale for a highly-heterogeneous medium is the focus of this research. The upscaling process itself has been examined in detail by Ahmadi et al. [20] and Cherblanc et al. [40], and the results of those efforts are summarized below. The focus of this paper is primarily on comparing theory and experiment for this second level of upscaling.

3.1.1. Microscale transport equations

We begin by posing the solute conservation equations in these two regions completed with boundary conditions (also, ultimately, arising from conservation equations; cf. Ref. [63]) at the $\eta-\omega$ interface. The Darcy-scale equations can be written similarly to those for the Darcy-scale numerical analysis described in Section 2.4.

η-region transport equation:

$$\varepsilon_\eta \frac{\partial c_\eta}{\partial t} + \nabla\cdot(\varepsilon_\eta \mathbf{v}_\eta c_\eta) = \nabla\cdot[\varepsilon_\eta \mathbf{D}_\eta^*\cdot\nabla c_\eta] \quad \text{in the } \eta\text{-region} \tag{27}$$

Boundary condition 1 (*equal concentrations at region interfaces*)

$$c_\eta = c_\omega \quad \text{at } A_{\eta\omega} \tag{28}$$

Boundary condition 2 (*equal fluxes at region interfaces*)

$$-\mathbf{n}_{\eta\omega}\cdot(\varepsilon_\eta \mathbf{v}_\eta c_\eta - \varepsilon_\eta \mathbf{D}_\eta^*\cdot\nabla c_\eta) = -\mathbf{n}_{\eta\omega}\cdot(\varepsilon_\omega \mathbf{v}_\omega c_\omega - \varepsilon_\omega \mathbf{D}_\omega^*\cdot\nabla c_\omega) \quad \text{at } A_{\eta\omega} \tag{29}$$

ω-region transport equation

$$\varepsilon_\omega \frac{\partial c_\omega}{\partial t} + \nabla\cdot(\varepsilon_\omega \mathbf{v}_\omega c_\omega^*) = \nabla\cdot[\varepsilon_\omega \mathbf{D}_\omega^*\cdot\nabla c_\omega] \quad \text{in the } \omega\text{-region} \tag{30}$$

Boundary condition 3 (*volume boundaries*):

$$c_\eta = F(t) \quad \text{at } A_{\eta e} \tag{31}$$

Initial conditions:

$$c_\eta = I_\eta(\mathbf{x}) \quad \text{in the } \eta\text{-region} \tag{32}$$

$$c_\omega = I_\omega(\mathbf{x}) \quad \text{in the } \omega\text{-region} \tag{33}$$

The parameters defined here are the same as for the Darcy scale equations reported in Section 2.4. Now, however, we have put general volume boundary and initial conditions on the system. To simplify the analysis, we will assume as in [20,40] that we can neglect variations of ε_η and ε_ω within the averaging volume (although ε_η and ε_ω themselves may be different from one another).

3.1.2. Upscaling

The upscaling is conducted by forming spatial averages over the (macroscale) averaging volume $\mathscr{V}$. The superficial and intrinsic averages for the concentration in the η- and ω-regions are given by

$$\langle c_\eta\rangle = \frac{1}{\mathscr{V}}\int_{V_\eta} c_\eta \,\mathrm{d}V, \quad \langle c_\eta\rangle^\eta = \frac{1}{V_\eta}\int_{V_\eta} c_\eta \,\mathrm{d}V \tag{34}$$

$$\langle c_\omega\rangle = \frac{1}{\mathscr{V}}\int_{V_\omega} c_\omega \,\mathrm{d}V, \quad \langle c_\omega\rangle^\omega = \frac{1}{V_\omega}\int_{V_\omega} c_\omega \,\mathrm{d}V \tag{35}$$

Here V_η is the volume of the η-region contained in the averaging volume $\mathscr{V}$. Similar definitions hold for the averages of the velocities $\mathbf{v}_\eta$ and $\mathbf{v}_\omega$. The intrinsic and superficial averages are linked, in analogy with the superficial and intrinsic averages posed at the pore scale, through the volume fraction of the region

$$\langle c_\eta\rangle = \varphi_\eta \langle c_\eta\rangle^\eta \tag{36}$$

$$\langle c_\omega\rangle = \varphi_\omega \langle c_\omega\rangle^\omega \tag{37}$$

Here we have used the following definitions for the volume fractions of the two regions

$$\varphi_\eta = V_\eta/\mathscr{V} \tag{38}$$

$$\varphi_\omega = V_\omega/\mathscr{V} \tag{39}$$

It is important to make the distinction between ε_β, which is the porosity of the Darcy-scale averaging volume (Level I of Fig. 1), and the volume fractions φ_η and φ_ω, which represent the fractions of high- and low-conductivity regions respectively (Level II of Fig. 1).

In addition to the definition of the averages and the volume fractions, one additionally needs a theorem describing

how to interchange the operations of averaging and differentiation when discontinuities at the phase boundaries are present. The required theorem is known as the spatial averaging theorem, and it has been derived by various researchers in a variety of ways [63–68]. The spatial averaging theorem can be stated

$$\langle \nabla c_\eta \rangle = \nabla \langle c_\eta \rangle + \frac{1}{\mathscr{V}} \int_{A_{\omega\eta}} \mathbf{n}_{\eta\omega} c_\eta \, \mathrm{d}V \tag{40}$$

where $\mathbf{n}_{\eta\omega}$ represents the unit normal pointing from outward from the η-region. Finally, in the process of averaging, one always finds terms involving the Darcy-scale values (which we refer to also as the 'point' values even though a Darcy-scale support volume is assumed) of c_η, c_ω, $\mathbf{v}_\eta$, and $\mathbf{v}_\omega$ rather than their averages. It is often useful to express these terms as the sum of an average plus a deviation quantity, i.e.,

$$c_\eta(\mathbf{x},t) = \langle c_\eta \rangle^\eta \big|_{\mathbf{x},t} + \tilde{c}_\eta(\mathbf{x},t) \tag{41}$$

$$c_\omega(\mathbf{x},t) = \langle c_\omega \rangle^\omega \big|_{\mathbf{x},t} + \tilde{c}_\omega(\mathbf{x},t) \tag{42}$$

$$\mathbf{v}_\eta(\mathbf{x}) = \langle \mathbf{v}_\eta \rangle^\eta \big|_{\mathbf{x}} + \tilde{\mathbf{v}}_\eta(\mathbf{x}) \tag{43}$$

$$\mathbf{v}_\omega(\mathbf{x}) = \langle \mathbf{v}_\omega \rangle^\omega \big|_{\mathbf{x}} + \tilde{\mathbf{v}}_\omega(\mathbf{x}) \tag{44}$$

Elimination of the deviation terms by expressing them as functions of the concentration averages is classically known as the closure problem. The closure problem will be discussed in additional detail below and in Appendix A. In the remainder of the paper we will drop the explicit reference to the coordinates, with the understanding that each of these quantities (point value, the mean, and the deviation) are treated as fields that are defined uniquely pointwise.

With these definitions one can derive large-scale averaged equations at the macroscopic scale (Level II of Fig. 1) by applying the averaging operators to the Darcy-scale conservation equations posed by Eqs. (27)–(33). The development of the two-equation model by averaging Eqs. (27)–(33) has been presented previously [20,40], and we simply list the result here

η-region:

$$\underbrace{\frac{\partial \langle c_\eta \rangle^\eta}{\partial t}}_{\text{Accumulation}} = \underbrace{\nabla \cdot [\mathbf{D}^*_{\eta\eta} \cdot \nabla \langle c_\eta \rangle^\eta]}_{\text{Dispersion}} - \underbrace{\langle \mathbf{v}_\eta \rangle^\eta \cdot \nabla \langle c_\eta \rangle^\eta}_{\text{Convection}} - \underbrace{\varepsilon_\eta^{-1} \varphi_\eta^{-1} \alpha^* (\langle c_\eta \rangle^\eta - \langle c_\omega \rangle^\omega)}_{\text{Inter-phase mass transfer}} + \underbrace{\varepsilon_\eta^{-1} \varphi_\eta^{-1} \Omega_\eta}_{\text{Non-conventional terms}} \tag{45}$$

ω-region:

$$\underbrace{\frac{\partial \langle c_\omega \rangle^\omega}{\partial t}}_{\text{Accumulation}} = \underbrace{\nabla \cdot [\mathbf{D}^*_{\omega\omega} \cdot \nabla \langle c_\omega \rangle^\omega]}_{\text{Dispersion}} - \underbrace{\langle \mathbf{v}_\omega \rangle^\omega \cdot \nabla \langle c_\omega \rangle^\omega}_{\text{Convection}} + \underbrace{\varepsilon_\omega^{-1} \varphi_\omega^{-1} \alpha^* (\langle c_\eta \rangle^\eta - \langle c_\omega \rangle^\omega)}_{\text{Inter-phase mass transfer}} + \underbrace{\varepsilon_\omega^{-1} \varphi_\omega^{-1} \Omega_\omega}_{\text{Non-conventional terms}} \tag{46}$$

We have used the following definitions for the effective parameters:

$$\mathbf{D}^*_{\eta\eta} = \frac{1}{V_\eta} \int_{V_\eta} [\mathbf{D}^*_\eta \cdot (\mathbf{I} + \nabla \mathbf{b}_{\eta\eta}) - \tilde{\mathbf{v}}_\eta \mathbf{b}_{\eta\eta}] \mathrm{d}V \tag{47}$$

$$\mathbf{D}^*_{\omega\omega} = \frac{1}{V_\omega} \int_{V_\omega} [\mathbf{D}^*_\omega \cdot (\mathbf{I} + \nabla \mathbf{b}_{\omega\omega}) - \tilde{\mathbf{v}}_\omega \mathbf{b}_{\omega\omega}] \mathrm{d}V \tag{48}$$

$$\begin{aligned} \alpha^* &= -\frac{1}{\mathscr{V}} \int_{A_{\eta\omega}} \mathbf{n}_{\eta\omega} \cdot (\varepsilon_\eta \mathbf{v}_\eta r_\eta - \varepsilon_\eta \mathbf{D}_\eta \cdot \nabla r_\eta) \mathrm{d}A \\ &= \frac{1}{\mathscr{V}} \int_{A_{\eta\omega}} \mathbf{n}_{\eta\omega} \cdot (\varepsilon_\omega \mathbf{v}_\omega r_\omega - \varepsilon_\omega \mathbf{D}_\omega \cdot \nabla r_\omega) \mathrm{d}A \end{aligned} \tag{49}$$

The variables $\mathbf{b}_{\eta\eta}$, $\mathbf{b}_{\omega\omega}$, r_η, and r_ω are specified by the solution to a set of three closure problems, and this process is described more fully in Appendix A. Note that the velocity appears as a parameter field. The balance equations for the momentum itself is not upscaled (this would lead to a large-scale form of Darcy's law), nor is it needed for predicting the effective dispersion tensor. This is common to all theories of upscaling of the dispersion problem; the effective dispersion tensor is defined by integrals of the microscale velocity field. Finally, we note that these equations represent the spatially smoothed mass balances that apply to a suitably sized volume that contains both matrix and inclusions. Although the ω-phase in the system that we describe is not connected at the microscale, the macroscale equations still contain both convection and dispersion terms; this is consistent with other similar formulations [20,42,46,69]. The proper way to think about this is that these equations honor the first and second moments of the solute transport within the two regions. The average ω-phase concentration, $\langle c_\omega \rangle^\omega$, has a first and second spatial moment that changes in time as the solute moves through the system. As pointed out by Kitanidis [70], the dispersion tensor only describes how solute spreads spatially, but it says essentially nothing about the spatial structure (or mixing) of the solute. The dispersion term in this case reflect the spatial spreading of the macroscale concentration, and says nothing else about how the concentration is organized within the volume of interest.

In Eqs. (45) and (46), the interaction between the two porous media is characterized by an inter-phase mass flux that is defined in terms of a macroscopic mass transfer coefficient, α^*, and the difference in concentration between the two regions. Unlike many 'two-region' models, there are also additional non-conventional flux terms, $\varepsilon_\eta^{-1}\varphi_\eta^{-1}\Omega_\eta$ and $\varepsilon_\omega^{-1}\varphi_\omega^{-1}\Omega_\omega$, that arise in the upscaling analysis; these are discussed more fully in Appendix A and by Cherblanc et al. [40]. For the conditions reported in this paper, we have verified that these non-conventional terms are negligible, and they are not considered further.

In general, the effective parameters that appear in Eqs. (47)–(49) are time-dependent. Several semi-heuristic theories have been developed to account for a non-local-in-time mass transfer coefficient [3,38]. However, linear transport models appear almost uniformly in practice, even though it is generally recognized that they are applicable for only a narrow range of conditions (e.g. [28,33,36,71]).

Generally, the development of the two-region model presented above requires a separation of space and time scales, which can be generically specified by

$$\ell_\eta, \ell_\omega \ll R_0 \ll L \tag{50}$$

$$t_\eta, t_\omega \ll T_\eta^* \tag{51}$$

where t_η and t_ω represent the characteristic time scales associated with the small length scales ℓ_η and ℓ_ω, and T_η^* is the time scale associated with macroscopic concentration changes in the high conductivity phase (the η-phase). Note that in particular, Eq. (51) is a somewhat crude simplification of this problem, which is characterized by many time scales (cf. [22]). However, to our knowledge, no thorough examination of the constraints required to ensure a separation of time scales in such highly heterogeneous media has yet been developed.

The effective coefficients which appear in Eqs. (45) and (46) are given explicitly by the set of three steady-state closure problems developed previously [20,40]. By definition, the solution to the steady state closure problems cannot recover all the eigenvalues that occur in the full transient closure problem. The closure problems described in Appendix A will be most accurate when the process time scales of the two regions are of the same order of magnitude. As the process time scale for the ω-phase (inclusions) becomes large relative to the time scale associated with the η-phase, the approximation of a steady-state closure becomes less accurate. Under these conditions, the use of a constant effective mass transfer parameter may not be valid [32]. It has been demonstrated by Landereau et al. [72] that the steady closure provides an approximation that is related to the harmonic mean of the eigenvalues (and the same result is obtained for the exchange coefficient provided by a Laplace transform analysis [72]).

3.2. Mixed model formulation

One method for improving the representation of the mass transfer process is to adopt the use of a distribution of relaxation times rather than a single time associated with the harmonic mean. This is the idea behind *multi-rate* models [3,22]. Multi-rate model represents the Laplacian operator as an eigenvalue expansion, and they keep a (potentially infinite) number of eigenvalues in this expansion as an approximation to the solution. This supplementary set of eigenvalues of the Laplacian operator forms a set of additional mass transfer coefficients. In essence, one can think of these models as adding additional regions to the system, where mass transfer in each region is described by a first-order mass transfer coefficient independent from the others. Considerable improvements have been obtained by this kind of approach (e.g. [72]), and it has been shown that for the 'mobile–immobile' model this representation converges to the case where mass transport in the immobile region is modeled explicitly as a diffusion process [22].

The construction of a multi-rate model is still not without difficulties, the foremost of which is that concentration in each additional region is defined by a transport equation that is fully coupled to each of the other regions. The complexity of this set of equations increases dramatically as the number of eigenvalues kept is increased. As an alternative to this approach, the idea of using a *mixed model* has been suggested by some researchers. In a mixed model, the macroscale description of mass transport is maintained for the matrix (the η-phase), but mass transfer for the inclusions is modeled at the microscale. The idea of mixed models for describing flow in dual-porosity media was introduced first for the case of the flow of a slightly compressible fluid in a two region medium (see a discussion of the literature in Ref. [73]). For dispersion problem, this idea was first proposed by Rao [74] and Bibby [75] and others [76,77], who applied the method to the problem of solute diffusion into (or out of) low conductivity regions during transport in a higher conductivity material. In the work of Rao [74], an finite difference solution for the concentration in a spherical inclusion was applied as 'sink' term to represent the influence of spherical inclusions in a high-conductivity matrix material. Improvements were observed for this mixed model when compared with the use of a conventional two-equation mass transfer model with a constant, but theoretically derived [78], coefficient. In the case of the work of Bibby [75], the applications were for a fracture-matrix network, and a solution was sought that only required that the statistics of the structure (in Bibby's case, these statistics were the average matrix block size, block porosity, joint spacing, and joint width) be maintained (cf. [79]).

We explore the use of a mixed model formulated in the spirit of the work of Rao [74] and Bibby [75]. The primary purpose for examining the mixed model is to provide some indication as to how much influence the quasi-steady assumption used in the prediction of α^* has on the resulting macroscale predictions. Because the mixed model maintains the eigenvalues associated with the diffusion problem, it is equivalent to a version of the multi-rate models discussed above. It also allows us a direct assessment of how important these eigenvalues are to the resulting macroscale solute transport behavior.

Our mixed model is developed by upscaling the transport equation for the η-region while the microscale representation is adopted for the ω-region. The mixed model takes the form

η-region:

$$\underbrace{\frac{\partial \langle c_\eta \rangle^\eta}{\partial t}}_{\text{Accumulation}} = \underbrace{\nabla \cdot [\mathbf{D}^*_{\eta\eta,mixed} \cdot \nabla \langle c_\eta \rangle^\eta]}_{\text{Dispersion}} - \underbrace{\langle \mathbf{v}_\eta \rangle^\eta \cdot \nabla \langle c_\eta \rangle^\eta}_{\text{Convection}} + \underbrace{\frac{\varepsilon_\eta^{-1} \varphi_\eta^{-1}}{V_\eta} \int_{A_{\omega\eta}} \mathbf{n}_{\eta\omega} \cdot (\varepsilon_\eta \mathbf{D}^*_\eta \nabla c_\eta)\, \mathrm{d}A}_{\text{Interfacial flux}} \tag{52}$$

ω-region:

$$\varepsilon_\omega \frac{\partial c_\omega}{\partial t} = \nabla \cdot [\varepsilon_\omega \mathbf{D}^*_\omega \cdot \nabla c_\omega] \tag{53}$$

and the following boundary conditions, derived from Eqs. (28) and (29), fully specify the boundary value problem

Boundary condition 1 (*equal concentrations*):

$$c_\omega = \langle c_\eta \rangle^\eta \quad \text{at } A_{\eta\omega} \tag{54}$$

Boundary condition 2 (*equal fluxes*):

$$\mathbf{n}_{\eta\omega} \cdot (\varepsilon_\eta \mathbf{D}^*_\eta \cdot \nabla c_\eta) = \mathbf{n}_{\eta\omega} \cdot (\varepsilon_\omega \mathbf{D}^*_\omega \cdot \nabla c_\omega) \quad \text{at } A_{\eta\omega} \tag{55}$$

Initial condition:

$$c_\eta = c_{\eta 0}, \quad c_\omega = c_{\omega 0} \quad \text{at } t = 0 \tag{56}$$

Implicitly this model assumes that convection in the ω-phase is negligible, and this approximation is valid for large values of the hydraulic conductivity ratio, κ.

The expression of the dispersion tensor $\mathbf{D}^*_{\eta\eta,\text{mixed}}$ which appears in Eq. (52) is derived by following the same development than for the two-equation model. In the development of the mixed model, however, the deviation term $\tilde{\mathbf{c}}_\eta$ is neglected at the interface, $A_{\eta\omega}$, which forces the solutions in the η- and the ω-regions to be uncoupled. Under these conditions, the dispersion tensor that is developed corresponds to a porous medium where the inclusions are impermeable. However, when the ratio of hydraulic conductivities, κ, is high, this approximation is a good one, and results in very little error. Following the developments detailed in Appendix B, the closure problem for the variable $\mathbf{b}_\eta$ can be expressed as follows:

Problem I. (*Closure problem related to the source* $\nabla \cdot \langle c_\eta \rangle^\eta$)

$$\nabla \cdot (\mathbf{u}_\eta \mathbf{b}_\eta) + \tilde{\mathbf{u}}_\eta = \nabla \cdot (\mathbf{D}'_\eta \cdot \nabla \mathbf{b}_\eta) + \nabla \cdot \widetilde{\mathbf{D}}'_\eta - \varphi_\eta^{-1} \mathbf{c}_{\eta,\text{mixed}} \tag{57}$$

$$B.C.1 \quad \mathbf{b}_\eta = 0 \quad \text{at } A_{\eta\omega} \tag{58}$$

$$B.C.2 \quad \mathbf{n}_{\eta\omega} \cdot (\mathbf{D}'_\eta \cdot \nabla \mathbf{b}_\eta) = 0 \quad \text{at } A_{\eta\omega} \tag{59}$$

$$\mathbf{b}_\eta(\mathbf{r} + \ell_i) = \mathbf{b}_\eta(\mathbf{r}), \quad i = 1, 2, 3 \tag{60}$$

$$\langle \mathbf{b}_\eta \rangle^\eta = 0 \tag{61}$$

where the constant is defined by

$$\mathbf{c}_{\eta,\text{mixed}} = -\frac{1}{\mathscr{V}} \int_{A_{\eta\omega}} \mathbf{n}_{\eta\omega} \cdot (\mathbf{u}_\eta \mathbf{b}_\eta - \mathbf{D}'_\eta \cdot \nabla \mathbf{b}_\eta - \mathbf{D}'_\eta) \mathrm{d}A \tag{62}$$

An expression similar to Eq. (47) is thus obtained for the effective coefficient,

$$\mathbf{D}^*_{\eta\eta,\text{mixed}} = \frac{1}{\mathscr{V}_\eta} \int_{V_\eta} [\mathbf{D}^*_\eta \cdot (\mathbf{I} + \nabla \mathbf{b}_\eta) - \tilde{\mathbf{v}}_\eta \mathbf{b}_\eta] \mathrm{d}V \tag{63}$$

In principle, this problem specification still requires that the interface between the two regions be explicitly known. This requirement means that the problem described by Eqs. (52)–(55) would be nearly as complex as the original problem described at the Darcy scale. However, if one can assume that the influence of the inclusions are independent from one another, and that the geometry of the inclusions is relatively constant, then it may be possible to represent the effects of the inclusions by examining a geometrically simplified representation of the system. Thus, the complexity of the porous medium is reduced to one or several representative unit cells. In this way, important transient information (representing the influence of particular eigenvalues of the solution) is kept, but a substantial reduction in the complexity of the system can be achieved. Based on the size and the distribution of the inclusions inside the flowcell, ten independent inclusions have been used to describe the domain. Thus, the concentration distribution in the η-phase, solved as a 1-dimensional problem, is coupled with the fine description of the 2-dimensional microscopic problem in the ω-region. The information transfer between both regions is processed through the interfacial flux, Eq. (52) and the boundary condition, Eq. (54).

4. Macroscale solutions

In the previous section, two different methods were proposed for developing a set of macroscale solute transport equations for highly heterogeneous (multi-region) media. Each of the models represents a form of upscaling, with the first-order mass transfer model being the more restrictive of the two. In applications to the experimental results, the solution to the macroscale transport problem is completed in a sequence of steps as follows.

1. A representative unit cell is identified for representing the important geometrical features of the heterogeneous porous medium. In principle, the unit cell can be as complex as we like, but it is preferable to search for a unit cell that tends to minimize the amount of complexity needed to recover the essential physics of the process of interest. There are no *a priori* rules for selecting a unit cell structure, since the complexity of the structure within the cell will depend both upon the actual physical structure of the porous medium that is being represented, and on the kinds of operators that are involved in the transport process itself. As an example, for pure diffusion in an isotropic medium, a simple periodic array of spheres in cubes [80] provides results that are very accurate when compared with the available laboratory data [81]. The same is not true, however, for the problem of dispersion in porous media, where the convection operator dramatically changes the nature of the transport problem. Ultimately, the selection of how much *information* must be contained in a unit cell must be done heuristically.
2. The closure problem (Appendix B) is solved over the representative unit cell to predict the fields $\mathbf{b}_{\eta\eta}$, $\mathbf{b}_{\omega\omega}$, r_η, and r_ω. The effective macroscale parameters defined by Eqs. (47)–(49) is obtained by numerical quadrature of these fields.

3. Once the effective parameters are determined, they are then used in a forward mode to predict the macroscale behavior of the heterogeneous system. This is done by solving the macroscale transport equations (given by Eqs. (45)–(49) for the first-order mass transfer model and by Eqs. (52)–(56) for the mixed model), augmented with the appropriate macroscale initial and boundary conditions, over the domain of interest. Velocities of each region are derived directly from the injection velocity. In this case, the observable macroscale behavior is measured by the breakthrough curves observed for the flowcells during each of the four experiments that were conducted.

Note that the goal of this effort is, ultimately, to produce a representation of the complex transport problem that contains fewer degrees of freedom than the original Darcy scale description. By definition, the first-order mass transfer model contains less information (fewer degrees of freedom) than does the mixed model. Correspondingly, however, the linear mass-transfer model has more stringent constraints on its validity, and we do not expect it to perform as well as the representation that contains a full diffusion model for transport in the inclusions. The details associated with completing these two steps are outlined below.

4.1. Calculation of the effective coefficients

Once characteristics of the unit cell are established, the closure problem consists in solving the sets of equations presented in Appendix B and calculating the associated large-scale coefficients. We used a flux continuous, locally conservative finite volume scheme that accommodated the use of full dispersion tensors [60]. This approach yielded an accurate approximation of the diffusion term, requiring nine-point support in 2-D. In this approach, the convection term is first treated using an ordinary upstream weighting scheme. The numerical dispersion introduced by this first-order scheme is then limited by locally correcting the diffusion term as described by Cherblanc et al. [40]. Finally the resulting linear system was solved using an successive over relaxation iteration algorithm. Once the mapping variables were computed, calculating the effective properties was done using Gaussian quadrature to compute the integrations that appear in Eqs. (47)–(49).

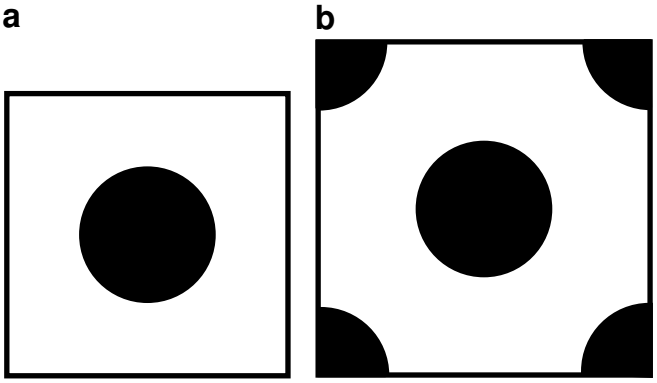

Fig. 6. Unit cells used for the solution to the closure problem: (a) square array and (b) staggered array.

Our initial computations of the effective parameters were computed using the simple unit cell illustrated in Fig. 6a. The volume fraction of each region as well as the size and the shape of the inclusion are identical to those used in the physical experiment. The effective parameters computed using this unit cell are presented in Table 2.

4.2. Macroscale simulations

Once the effective parameters had been determined from the solution to the closure problem (49), we then used these parameters to conduct a forward simulation of the flowcell using the upscaled equations given by Eqs. (45) and (46). Recall that these homogenized equations take the form of a two-region model where the geometry of the two regions are no longer represented explicitly. This forward simulation was a simple 1-dimensional solution to Eqs. (45) and (46) using the boundary conditions that were applicable to the experimental system. A comparison of the observed data and simulation results for the high and low hydraulic conductivity contrast cases, each for two different flow rates, appears as Figs. 7 and 8. One can see from these figures that the first part of the breakthrough curve from the large-scale computation lags the actual breakthrough curve, especially for the high conductivity contrast system.

Although in general it is the flux-averaged concentration that is measured at the flowcell effluent rather than the volume-averaged concentration, we were able to show that for the conditions of these experiments, the differences between

Table 2
Effective parameters computed from the numerical solution to the closure problem

Parameter	High contrast, $\kappa = 1800$		Low contrast, $\kappa = 300$	
	High flow rate ($Q = 1.32$ mL/min)	Low flow rate ($Q = 0.66$ mL/min)	High flow rate ($Q = 1.26$ mL/min)	Low flow rate ($Q = 0.63$ mL/min)
$D_{\eta\eta,xx}$, m^2/s	3.27×10^{-7}	1.63×10^{-7}	2.40×10^{-7}	1.20×10^{-7}
$D_{\omega\omega,xx}$, m^2/s	3.95×10^{-10}	3.82×10^{-10}	4.42×10^{-10}	4.04×10^{-10}
α^*, m/s	3.25×10^{-6}	2.96×10^{-6}	7.22×10^{-6}	4.56×10^{-6}
$\langle \mathbf{v}_\eta \rangle^\eta$, m/s	3.33×10^{-5}	1.67×10^{-5}	3.16×10^{-5}	1.58×10^{-5}
$\langle \mathbf{v}_\omega \rangle^\omega$, m/s	2.10×10^{-8}	1.04×10^{-8}	1.19×10^{-7}	5.94×10^{-8}

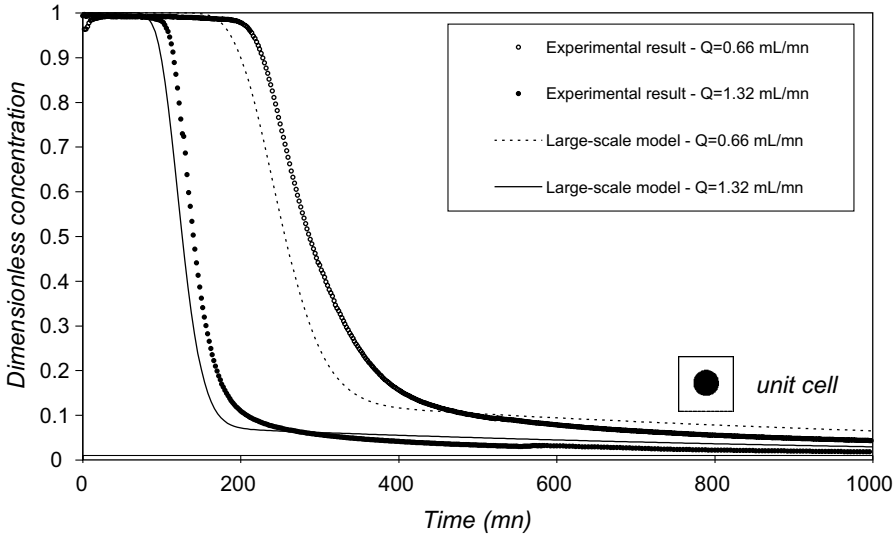

Fig. 7. Comparison of experimental data (points) and large scale simulations for the intermediate-contrast ($\kappa = 300$) case using the effective parameters determined by the solution to the steady closure problem with a simple unit cell.

these two quantities was negligible. To start, we noted that the flux-averaged concentration, $c_{\eta,\text{effluent}}$, can be written as

$$c_{\eta,\text{effluent}} = \frac{\int_{A_{\eta,\text{effluent}}} \mathbf{n}_{\eta e} \cdot (\mathbf{v}_\eta c_\eta)\, \mathrm{d}A}{\int_{A_{\eta,\text{effluent}}} \mathbf{n}_{\eta e} \cdot \mathbf{v}_\eta\, \mathrm{d}A} \tag{64}$$

The concentration in the integral can be decomposed using Eq. (41). Under the length scale constraints that have already been imposed, the average concentration can be taken out from under the integral yielding the following decomposition for $c_{\eta,\text{effluent}}$:

$$c_{\eta,\text{effluent}} = \langle c_\eta \rangle^\eta + c'_\eta \tag{65}$$

where

$$c'_\eta = \frac{\int_{A_{\eta,\text{effluent}}} \mathbf{n}_{\eta e} \cdot (\mathbf{v}_\eta \tilde{c}_\eta)\mathrm{d}A}{\int_{A_{\eta,\text{effluent}}} \mathbf{n}_{\eta e} \cdot \mathbf{v}_\eta\, \mathrm{d}A} \tag{66}$$

For the $\kappa = 1800$ case with $Q = 0.66$ mL/min, we found that the second term on the right-hand side of Eq. (65) was only a few percent of the spatial average concentration, $\langle c_\eta \rangle^\eta$. Although the deviation c'_η might be important in some instances, it was clearly not a major contribution to the differences between the experiments and theory that can be observed in Figs. 7 and 8.

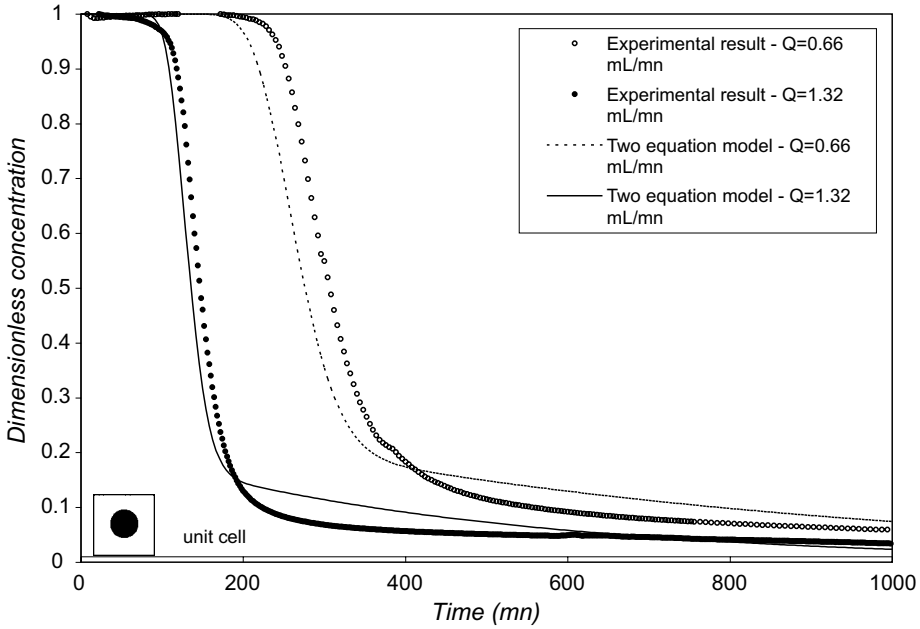

Fig. 8. Comparison of experimental data (points) and large scale simulations for the high-contrast ($\kappa = 1800$) case using the effective parameters determined by the solution to the steady closure problem with a simple unit cell.

5. Discussion

The comparison between the first-order mass transfer theory and the experimental breakthrough curves illustrated in Figs. 7 and 8 show a reasonable comparison; however, some significant differences also appear. The most significant difference is that the first-order mass transfer theory over-predicts the concentration at early time, and under-predicts the concentration at late time. This kind of behavior has been noted by other researchers [30], and ultimately it arises because the first-order mass transfer model matches only the first two moments of the breakthrough curve [30]. This leads to the breakthrough of tracer in the high-conductivity matrix occurring somewhat earlier than is actually observed.

We have hypothesized that the differences between theory and experiment may have resulted primarily because of two simplifications that we made for solving the closure problem associated with the first-order mass transfer model. These are (1) the geometrical simplification assumed in the closure problem, and (2) the quasi-steady assumption used to solve the closure problem. The impact of each of these assumptions is explored in more detail below.

5.1. Impact of geometry

Ideally, one can pick a simple unit cell that contains the essential features of the system of interest without the need for the cell being overly geometrically complex. The geometry of a unit cell is ultimately specified by (1) the physics of the problem under investigation, and (2) the accuracy of the solution that is desired. As an example, for the process of pure diffusion in isotropic porous media, upscaling investigations have shown that it is primarily the volume fraction of the fluid phase that determines the effective diffusion tensor [56,81]. In contrast, for the problem of heat transfer in porous media, the volume fraction of the media, the media structure, and the contact geometry among the solid-phase particles can all influence the resulting effective dispersion tensor for heat transport [82,83]. Although some of the necessary features of unit cell have been studied in some detail [84], it is currently not possible to determine *a priori* what the necessary features are for the unit cell (i.e., how much geometrical information must be represented) for a particular set of processes of interest. Therefore, this question must be addressed heuristically, using guidance from previous studies. Note that this problem is not a function of the method used to conduct the upscaling, but rather is a function of the kinds of processes that are manifest at the microscale. Consider, as an example, the well-developed theories pertaining to field-scale dispersion for continuous but mildly heterogeneous hydraulic conductivity fields. For this case, several approaches based on perturbation techniques have yielded results that predict the ensemble average of the effective dispersion tensor. However, it is much more difficult to say how large a particular realization (i.e., a particular unit cell) must be so that the ensemble average dispersion tensor is observed for it with a high degree of confidence. For fields that are highly heterogeneous and discrete, it is not currently possible to predict exactly what features need to be captured by a unit cell.

To address this problem, we have examined the influence of three different unit cells of increasing complexity on the effective parameters computed from the closure problem. The first unit cell corresponds to the simple unit cell used previously, and is illustrated in Fig. 6a. The second unit cell, illustrated in Fig. 6b, has been made slightly more complex by imposing a staggered structure on the inclusions. If interactions among inclusions are particularly important, we would expect this staggered array to give a result that is different from that obtained for a simple unit cell. Finally, to determine unambiguously how much these two simplified unit cells impact the computation of the effective parameters, we have used a third unit cell that has all of the microscale geometry for the experimental system embedded in it (i.e., the unit cell is structured like the experimental distribution of hydraulic conductivities, as illustrated in Fig. 3). The volume fraction of the two regions, size, average separation distance between inclusions, and shape of the inclusions are identical for the three unit cells.

It should be noted that this last unit cell does not lead to an upscaling that is particularly useful, because the numbers of degrees of freedom in the upscaling problem are essentially equal to the number of degrees of freedom contained in the direct numerical solution at the Darcy scale as described in Section 4. However, the solution for this field is a useful reference for this investigation, because it provides a unique indication of the information content required by the closure problem. If the information content of the simple unit cells (Fig. 6) is sufficient, then the closure problem for each of these unit cells should give (within some acceptable error) the same answer. However, if the correlation structure of the experimental system is important (in that the specifics of interactions among inclusions are important), then it is unlikely that the simple unit cells will be sufficient. Although with simple periodic cells we can match the volume fraction and mean separation distance of the inclusions (the zeroth and first moments respectively), we cannot reproduce the correlation structure of the field (the second moment) with a simple periodic cell.

In Fig. 9 we have illustrated the impact of the pore-scale geometry on the elution curves obtained from the macroscale two-equation model for the high contrast medium and the flow rate of $Q = 0.66$ mL/min; this represents the case that previously lead to the most significant deviation between theory and experiment. The effective parameters computed for the staggered unit cell (unit cell 2) and the full domain (unit cell 3) are listed in Table 3.

The results of these simulations suggest that the complexity of the unit cell itself is not the source of the discrepancy between theory and experiment.

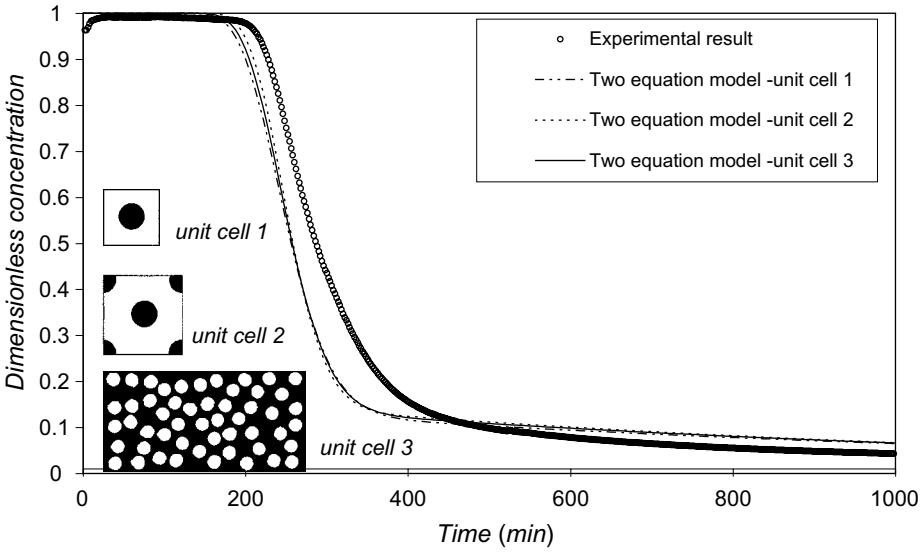

Fig. 9. Comparison between experimental results and two-equation model for different unit cells, high-contrast case, $Q = 0.66$ mL/min.

5.2. Steady closure assumption for prediction of α^*

The discussion above suggests that the discrepancy between theory and experiment must result from one or more of the assumptions imposed on the closure problem. Two primary assumptions are imposed on the closure problem that is described in Appendix B: (1) it is assumed that quasi-steady conditions can be imposed so that the time dependence of α^* can be neglected, and (2) it is assumed that the difference of the average quantities can be treated as constant for the purposes of the closure problem. These two assumptions result in a *steady* closure problem that is *decoupled* from the macroscale transport equations. It is this assumption that ultimately leads us to a simple first-order approximation of the mass transfer coefficient within the two-equation model. Without this approximation, the fully transient closure would lead to a solution that takes the form of an integro-differential equation [42,85], equivalent to the multi-rate methods that have been described previously [22].

The influence of imposing the quasi-steady and decoupled conditions on the closure problem have been studied in some detail by Landereau et al. [72], and Cherblanc et al. [40]; however, a detailed understanding as to how α^* is influenced by this kind of closure is still unresolved.

Table 3
Comparison of effective parameters computed for three unit cells

Parameter	High contrast $\kappa = 1800$, $Q = 0.66$ mL/min		
	Unit cell 1	Unit cell 2	Unit cell 3
$D_{\eta\eta,xx}$, m^2/s	1.63×10^{-7}	1.11×10^{-7}	1.39×10^{-7}
$D_{\omega\omega,xx}$, m^2/s	3.82×10^{-10}	4.90×10^{-10}	3.84×10^{-10}
α^*, m/s	2.96×10^{-6}	3.29×10^{-6}	3.16×10^{-6}
$\langle \mathbf{v}_\eta \rangle^\eta$, m/s	1.67×10^{-5}	1.67×10^{-5}	1.67×10^{-5}
$\langle \mathbf{v}_\omega \rangle^\omega$, m/s	1.04×10^{-8}	1.02×10^{-8}	1.15×10^{-8}

We can make some progress by considering a special case of the two-equation model where it is assumed that (1) convective transport can be neglected within the inclusions (ω-phase), and (2) spatial concentration gradients in the matrix (η-phase) are negligible, and (3) the inclusions are uniform spheres (or cylinders in 2D) that are assumed to be non-interacting. The resulting model has been studied in detail by Rao et al. [78], and a fully transient expression for the mass transfer coefficient is available from that study. In our notation, the microscale formulation of the Rao problem takes the form

η-region transport equation

$$c_\eta = c_{\eta 0}(t) \quad \text{in the } \eta\text{-region} \tag{67}$$

Boundary condition:

$$c_\omega = c_{\eta 0}(t) \quad \text{at } A_{\eta\omega} \tag{68}$$

ω-region transport equation

$$\varepsilon_\omega \frac{\partial c_\omega}{\partial t} = \nabla \cdot [\varepsilon_\omega D^*_\omega \nabla c_\omega] \quad \text{in the } \omega\text{-region} \tag{69}$$

Initial condition

$$c_\eta = 0 \quad \text{at } t = 0 \tag{70}$$

$$c_\omega = c_{\omega 0} \quad \text{at } t = 0 \tag{71}$$

For this particular problem, Rao et al. [78] develop a closure for the transient mass transfer coefficient in terms of a pair of infinite series. The resulting solution for $\alpha^*(t)$ shows exponential decay to a well-defined asymptotic value as time tends toward infinity. This asymptotic value is

$$\alpha^* = \frac{\beta(\varphi_\omega)}{a^2} \varphi_\omega \varepsilon_\omega D^*_\omega \tag{72}$$

where the coefficient $\beta(\varphi_\omega)$ is approximately $10 \leqslant \beta(\varphi_\omega) \leqslant 20$ for $0 \leqslant \varphi_\omega \leqslant 1$.

It is interesting to note that when Eqs. (67)–(71) are subjected to the volume averaging procedure with a steady and

decoupled closure scheme, as described above, a different value for the asymptotic value of α^* is obtained. In Appendix C we have presented the details of this analysis, and one finds that for the Rao problem, the value of α^* predicted from our closure scheme is given by

$$\alpha^* = \frac{15}{a^2}\varphi_\omega \varepsilon_\omega D^*_\omega, \quad \text{3-D, spherical inclusions} \tag{73}$$

$$\alpha^* = \frac{8}{a^2}\varphi_\omega \varepsilon_\omega D^*_\omega, \quad \text{2-D, cylindrical inclusions} \tag{74}$$

and these results are consistent with a large number of studies [28–30,32,34]. It has been recognized previously [3,22] that these results represent the harmonic average of the eigenvalues of the closure problem, and this result is verified in the context of volume averaging in Appendix C.

In comparing the closure of Rao et al. [78] with the volume averaging scheme that we have presented, it is apparent that the discrepancy between the asymptotic values for α^* arises because of the decoupling of the microscale and macroscale transport problems. In other words, the macroscale variables ($\langle c_{A\eta}\rangle^\eta$, $\langle c_{A\omega}\rangle^\omega$, $\nabla\langle c_{A\eta}\rangle^\eta$ and $\nabla\langle c_{A\omega}\rangle^\omega$) are treated in our work (and in a large number of previous studies by other researchers) as being spatially and temporally constant for the purposes of the closure problem. In essence, this approximation forces the value of α^* to be the harmonic average of the eigenvalues of the closure problem.

The result that the steady decoupled closure scheme produces a harmonic-averaged value for α^* is a significant one. It has been shown by Harvey and Gorelick [30] that this choice for α^* assures that the zeroth, first, and second temporal moments of the breakthrough curve are maintained when one compares the exact and upscaled (i.e., first-order mass transfer) results. Recently, Ahmadi et al. [20] and Quintard et al. [19] have obtained similar but more general results for a mobile/mobile model developed in the context of volume averaging. These results illustrate that if one imposes that a first-order mass transfer model with constant α^* must be used, then the best possible (as measured by the zeroth, first, and second moments) value for α^* in the geometries investigated thus far (slabs, cylinders and spheres) is obtained by the steady, decoupled closure problem. This is identical to the closure scheme described in Appendix B, and, therefore, the values for α^* computed for this work are optimal in the sense of maintaining equivalence for these three moments.

The use of a constant value for α^* represents a tradeoff between reducing computational complexity and the accuracy of the final results. In the breakthrough curves shown in Figs. 7 and 8 it is clear that, although three moments of prediction and experimental data may be the same, pointwise there may still be substantial deviations between the two concentrations. This is because the third (skewness) and subsequent moments do not match, and, in fact, can not be made to match using a first-order mass transfer model with constant α^* [30]. If greater accuracy is desired, one could adopt the use of a fully transient closure problem with coupling between the macroscale and microscale concentrations. In general, this leads to a very complex problem that begins to be nearly as difficult (if not more so) than the direct solution

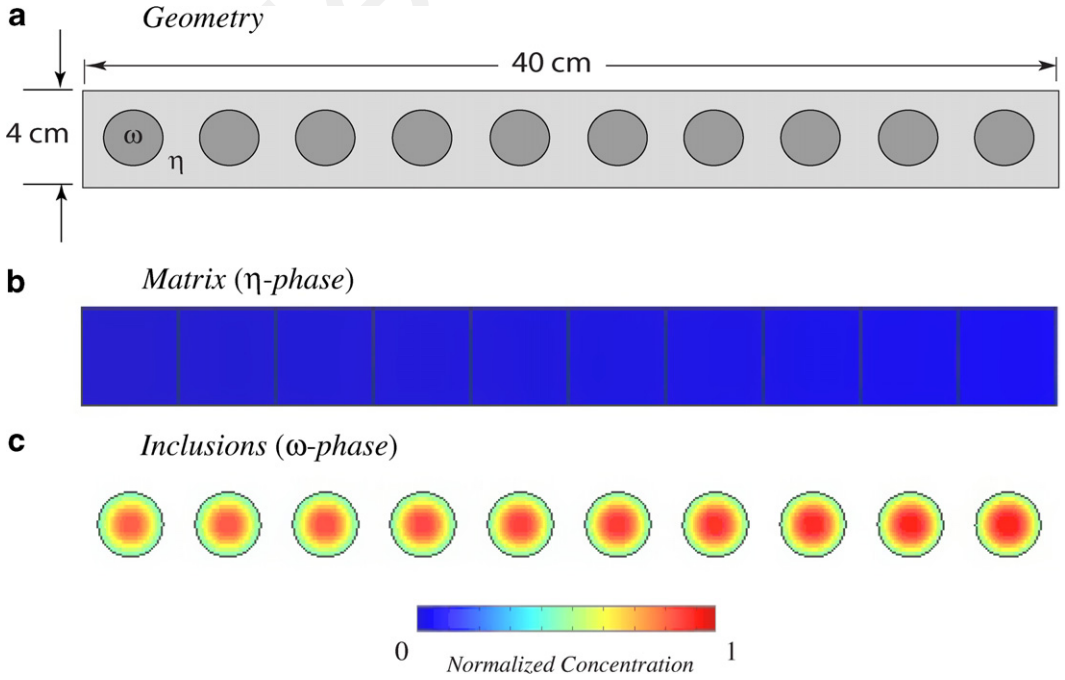

Fig. 10. Geometry and dimensionless concentration fields the simplified medium used in the mixed model. The concentration field is shown for $t = 500$ min for the low-flow-rate ($Q = 0.66$ mL/min) case.

to the problem at the microscale. Under some circumstances, in fact, one can consider using a direct solution for the concentration in the inclusions coupled with an upscaled description of transport in the matrix material. In fact, the result obtained by Rao et al. [78] can be considered to be of this type. In the next section, we briefly describe this approach, and provide some examples as to how it may be applied while still reducing the overall complexity of the problem under consideration.

5.3. Mixed model results

Fig. 10 shows the dimensionless concentration fields obtained from the mixed model for the low flow rate conditions ($Q = 0.66$ mL/min) for the intermediate-contrast case. Breakthrough curves for both cases appear in Figs. 11 and 12. Even for the intermediate-contrast case where the convection should be an important process (as can be seen in Fig. 5, where a small amount of asymmetry of the

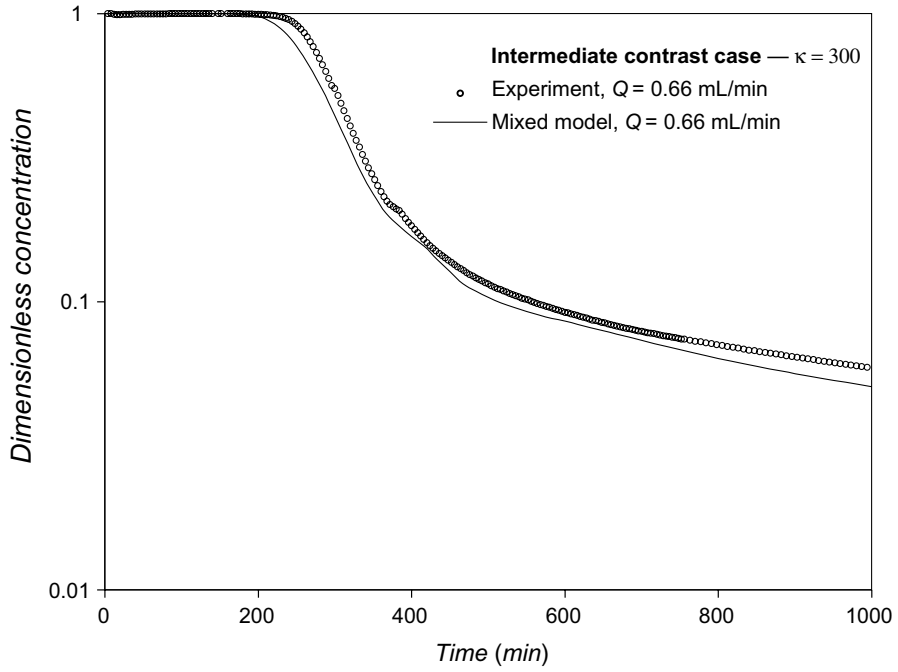

Fig. 11. Breakthrough curve for the mixed model, intermediate-contrast case (0.66 mL/mn).

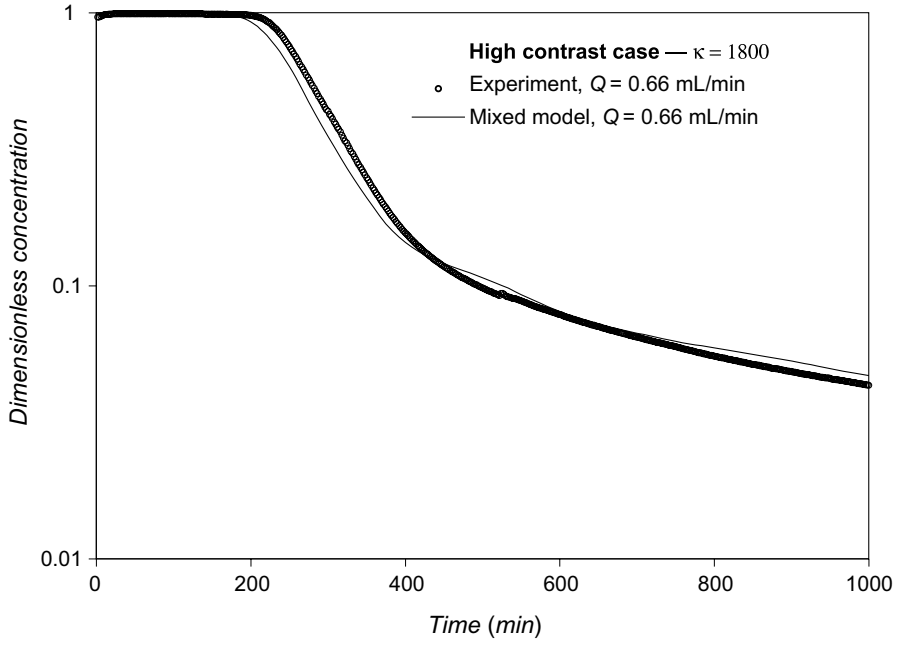

Fig. 12. Breakthrough curve for the mixed model, high-contrast case (0.66 mL/mn).

concentration field inside the inclusion can be observed due to convective effects), it is interesting to note that a mixed model still provides reasonably accurate results. The minor deviations that can be observed between theory and experiment result largely from the simplified geometry that has been adopted; however, in many instances the decrease in problem complexity would warrant this trade off.

These results show that the mixed model provides a substantially improved agreement between the experimental data and theory. This improvement does come at a cost: in the mixed model, essentially all of the eigenvalues associated with transport in the inclusions are kept, and the result is that more computational effort is required to compute the solution. One could argue that the simplified geometry that we have adopted could be used to directly solve the microscale equations as originally posed by Eqs. (27)–(33). Although in principle this is true, our use of the mixed model here is specifically formulated to better understand the impact that the steady-state approximation in the closure problem for the mass transfer coefficient imposes on the resulting macroscale equation described in Section 3. Two additional criticisms can be made regarding the use of the mixed model. First, the formulation of the dispersive tensor implies that this one takes only into account the passive dispersion. This can have a strong impact, especially in reactive mass transfer problems. Second, the two-equation model admits a small variation of the concentration at the interface and accounts for convective effects within the inclusions; these processes are not included in the mixed model as we have formulated it. Nevertheless, the mixed model represents another tool that can be used to examine the macroscale behavior of multi-scale systems.

6. Conclusions

In this work we have examined the *a priori* prediction of the effective mass transfer coefficient for a two-region medium using the method of volume averaging with steady closure. Various methods exist for predicting the effective mass transfer coefficient when diffusion dominates within low-conductivity regions and these regions have idealized (e.g. spherical, ellipsoidal, planar) geometries. However, relatively fewer methods have been developed to handle cases where the geometry is not necessarily ideal and where non-negligible convection may occur in the low-conductivity inclusions. The method that we have described does apply to these more general conditions, and allows for the computation of the effective mass transfer coefficient on the basis of the microscale physical properties and geometry of the media. From the results described in this work, our primary results and comments for future research on this problem are as follows:

1. The first-order mass transfer model can be developed via volume averaging, and the resulting theory allows one to predict the effective mass transfer coefficient through the solution of a closure problem. This closure can be done numerically, and the method is therefore not constrained to cylindrical or spherical geometries. The macroscale equations take the forms shown in Eqs. (1) and (2), and the effective parameters (the effective mass transfer coefficient, α^*, and the effective dispersion tensors $\mathbf{D}^*_{\eta\eta}$ and $\mathbf{D}^*_{\omega\omega}$) can be predicted from the closure problems described in Appendix B.
2. Our results indicate that the approach reasonably represents the mass transfer process when applied at the macro scale. However, the existence of a formal method for predicting the effective mass transfer coefficient does not eliminate the shortcomings of the first-order mass transfer model. These shortcomings have been discussed at some length by other researchers [3,22,28,30,36,37], and include (1) early arrival of the solute front, and (2) higher concentrations in the 'tailing' part of the effluent breakthrough curve for a step decrease in influent concentration.
3. For the special case where convection can be neglected in the low-conductivity inclusions, we have shown in Appendix C that the effective mass transfer coefficient, α^*, is equal to the harmonic average of the eigenvalues associated with the closure problem. For spherical and cylindrical inclusions, this result is consistent with previous observations [3,22,72], and leads to the classical result of $\alpha^* = \beta\varphi_\omega\varepsilon_\omega D^*_\omega/a^2$, where β is a parameter that depends upon the geometry of the system. It has been shown previously by Harvey and Gorelick [30] that for this case one can match the zeroth, first, and second temporal moments of the breakthrough curve using a linear mass transfer model with a constant mass transfer coefficient; however, higher-order moments cannot be matched. The volume averaging scheme that we have described yields the value of α^* that is identical to that proposed by Harvey and Gorelick [30]. This value of α^* can be said to be 'optimal' in the sense that it predicts the best possible value of α^* (as measured by adherence to honoring the first three moments of a breakthrough curve) for a linear mass transfer model with constant coefficients.
4. The utility of the steady closure scheme for predicting α^* will depend upon the degree of accuracy required for the macroscale transport equations. Although the closure scheme that we describe can be considered to be 'optimal' in the sense described by Harvey and Gorelick [30] for the spherical diffusion case, there are still obvious deviations between the observed breakthrough curves and those predicted by the macroscale theory (e.g. Figs. 7 and 8). For many applications, the reduction in complexity that a macroscale linear mass transfer model with a constant coefficient provides may be worth the trade-off of reduced accuracy when compared to the direct solution of the microscale equations.
5. For cases where the linear mass transport model with a constant coefficient does not provide sufficient accuracy, we have provided an example of a mixed model that can

provide improved representation of the inter-region transport process in the case where convection within low-conductivity regions can be neglected. The mixed model solves the macroscale transport equation in the matrix, but solves the microscale transport equation in the low-conductivity inclusions. The resulting equations can be solved in a representative domain that is substantially less complex than the full microscale geometry of the heterogeneous medium, leading to a substantial reduction in complexity when compared to the direct microscale solution. As shown in Figs. 11 and 12, the resulting description of the mass transport can be dramatically improved as compared with the results obtained using the macroscale equations with the steady closure scheme.

6. Our results (e.g. Fig. 9) have shown that simple unit cells can be used to predict accurate values for α^*, even for structurally complex media. This suggests that the value of α^* predicted from a steady closure scheme is primarily a function of (i) the volume fraction of the inclusions, (ii) the physical properties (hydraulic conductivity, porosity, and dispersivity), and (iii) the geometry of individual inclusions. Interactions among inclusions appear, at least for values of φ_ω near the values studied in this work, to be of secondary importance to the prediction of α^*.

Additional research should be conducted on upscaling schemes that can represent the *transient evolution* of the effective mass transfer coefficient. The disadvantage of this approach is that the transport equations will necessarily become non-local in time. However, if efficient approximations can be found, these might yield improved results at the macroscale without the need to directly compute the microscale solutions (as is done in the mixed model approach). The prediction of time-dependent mass transfer coefficients represents research that is currently in progress, and some first results are available in the publication by Chastanet and Wood [43].

Acknowledgements

This research was supported in part by the NSF (Collaborations in Mathematics and Geosciences) under Grant 0327578, and by Pacific Northwest National Laboratory under agreement 406640-A-N4/15325 ''Development of Volume Averaged Equations and Implementation of Numerical Solutions''.

Appendix A

In description of multi-scale systems, notation can be come unduly complex. In an effort to simplify the notation and yet still make it possible for the reader to be certain about the interpretation of various quantities, we list the following Darcy scale variables here in terms of the subpore scale averages over which they are defined. The following list contains Darcy scale variables defined by integrating over a representative volume (corresponding to the volume V_d in Fig. 1, Level III). In Fig. 1, Level III, the fluid phase is referred to as the 'β-phase'. The volume of the fluid phase within the averaging volume $\mathscr{V}_d$ is represented by $\mathscr{V}_{\beta,\eta}$ or $\mathscr{V}_{\beta,\omega}$, depending upon which region the volume V_d resides in.

Darcy scale porosity in the η- and ω-regions

$$\varepsilon_\eta = \frac{\mathscr{V}_{\beta,\eta}}{\mathscr{V}_d} \quad \text{in the } \eta\text{-region} \tag{A.1}$$

$$\varepsilon_\omega = \frac{\mathscr{V}_{\beta,\omega}}{\mathscr{V}_d} \quad \text{in the } \omega\text{-region} \tag{A.2}$$

Darcy scale intrinsic (average pore-scale) concentration in the η- and ω-regions

$$c_\eta = \frac{1}{V_{\beta,\eta}} \int_{V_{\beta,\eta}} c_\beta \, \mathrm{d}V \quad \text{in the } \eta\text{-region} \tag{A.3}$$

$$c_\omega = \frac{1}{V_{\beta,\omega}} \int_{V_{\beta,\omega}} c_\beta \mathrm{d}V \quad \text{in the } \omega\text{-region} \tag{A.4}$$

Darcy scale intrinsic (average pore-scale) velocity in the η- and ω-regions

$$\mathbf{v}_\eta = \frac{1}{V_{\beta,\eta}} \int_{V_{\beta,\eta}} \mathbf{v}_\beta \, \mathrm{d}V \quad \text{in the } \eta\text{-region} \tag{A.5}$$

$$\mathbf{v}_\omega = \frac{1}{V_{\beta,\omega}} \int_{V_{\beta,\omega}} \mathbf{v}_\beta \, \mathrm{d}V \quad \text{in the } \omega\text{-region} \tag{A.6}$$

Darcy scale total dispersion tensor

$$\mathbf{D}^*_\eta = \mathbf{D}_{eff,\eta} + \mathbf{D}_\eta \quad \text{in the } \eta\text{-region} \tag{A.7}$$

$$\mathbf{D}^*_\omega = \mathbf{D}_{eff,\omega} + \mathbf{D}_\omega \quad \text{in the } \omega\text{-region} \tag{A.8}$$

More information regarding the definition of the components of the dispersion tensor described by Eqs. (A.7) and (A.8) can be found in Ref. [56, Chapter 3].

Appendix B. The closure problem

In the process of volume averaging, one always finds integrals of the deviation concentrations in the averaged conservation equation. The process of determining the relationship between the deviations and the mean concentration is classically known as 'closure'. The closure problems associated with the two-equation model have been developed previously by Ahmandi et al. [20] and by Cherblanc et al. [40]. Briefly, one develops a conservation equation for the deviation concentrations by subtracting the phase-averaged equations from the Darcy-scale equations given by Eqs. (27) and (30) (this is analogous to how conservation equations for the Reynolds stress are developed in the theory of homogeneous turbulence). The boundary conditions given by Eqs. (28) and (29) are decomposed using Eqs. (41) and (42) to develop conditions that involve the deviation concentrations. At this point, one has conservation equations for the quantities $\tilde{c}_\eta$ and $\tilde{c}_\omega$ complete with

boundary conditions. The quantities $\nabla\langle c_\eta\rangle^\eta$, $\nabla\langle c_\omega\rangle^\omega$ and $(\langle c_\eta\rangle^\eta - \langle c_\omega\rangle^\omega)$ arise as non-homogeneous source terms in these equations.

Under the separation of length scales constraint posed by Eq. (50), spatial variations of the mean concentrations (and their gradients) can be neglected for the purposes of the closure problem (cf. Whitaker [56], Chapter 2). It is possible to show that for linear problems under these conditions, the solution of the problem must be a function of the source terms of the form (cf. Wood et al. [86] for an explicit 1-phase example)

$$\tilde{c}_\eta = \mathbf{b}_{\eta\eta}\cdot\nabla\langle c_\eta\rangle^\eta + \mathbf{b}_{\eta\omega}\cdot\nabla\langle c_\omega\rangle^\omega + r_\eta(\langle c_\eta\rangle^\eta - \langle c_\omega\rangle^\omega) \tag{B.1}$$

$$\tilde{c}_\omega = \mathbf{b}_{\omega\omega}\cdot\nabla\langle c_\omega\rangle^\omega + \mathbf{b}_{\omega\eta}\cdot\nabla\langle c_\eta\rangle^\eta + r_\omega(\langle c_\omega\rangle^\omega - \langle c_\eta\rangle^\eta) \tag{B.2}$$

With these functional forms established, one can show that three closure problems define the unknown functions $\mathbf{b}_{\eta\eta}$, $\mathbf{b}_{\eta\omega}$, $\mathbf{b}_{\omega\eta}$, $\mathbf{b}_{\omega\omega}$, r_η and r_ω.

In the following, we have made special efforts to keep the notation for the closure problem as similar to that used by Cherblanc et al. [40] as possible. To that end, we have adopted the following notation:

$$\mathbf{u}_\eta = \varepsilon_\eta\mathbf{v}_\eta \tag{B.3}$$

$$\mathbf{u}_\omega = \varepsilon_\omega\mathbf{v}_\omega \tag{B.4}$$

$$\mathbf{u}_\eta = \langle\mathbf{u}_\eta\rangle^\eta + \tilde{\mathbf{u}}_\eta \tag{B.5}$$

$$\mathbf{u}_\omega = \langle\mathbf{u}_\omega\rangle^\omega + \tilde{\mathbf{u}}_\omega \tag{B.6}$$

$$\mathbf{D}'_\eta = \varepsilon_\eta\mathbf{D}^*_\eta \tag{B.7}$$

$$\mathbf{D}'_\omega = \varepsilon_\omega\mathbf{D}^*_\omega \tag{B.8}$$

$$\mathbf{D}'_\eta = \langle\mathbf{D}'_\eta\rangle^\eta + \tilde{\mathbf{D}}'_\eta \tag{B.9}$$

$$\mathbf{D}'_\omega = \langle\mathbf{D}'_\omega\rangle^\omega + \tilde{\mathbf{D}}'_\omega \tag{B.10}$$

For the purposes of the closure problem only, we will also neglect variations in the volume fractions ε_η, ε_ω, φ_η, and φ_ω. With this notation, the closure problem can be stated as [40].

Problem I. (*Closure problem related to the source* $\nabla\cdot\langle c_\eta\rangle^\eta$)

$$\nabla\cdot(\mathbf{u}_\eta\mathbf{b}_{\eta\eta}) + \tilde{\mathbf{u}}_\eta = \nabla\cdot(\mathbf{D}'_\eta\cdot\nabla\mathbf{b}_{\eta\eta}) + \nabla\cdot\tilde{\mathbf{D}}'_\eta - \varphi_\eta^{-1}\mathbf{c}_{\eta\eta} \tag{B.11}$$

$$B.C.1 \quad \mathbf{b}_{\eta\eta} = \mathbf{b}_{\omega\eta} \quad \text{at } A_{\eta\omega} \tag{B.12}$$

$$B.C.2 \quad \mathbf{n}_{\eta\omega}\cdot(\mathbf{D}'_\eta\cdot\nabla\mathbf{b}_{\eta\eta}) = \mathbf{n}_{\eta\omega}\cdot(\mathbf{D}'_\omega\cdot\nabla\mathbf{b}_{\omega\eta}) \quad \text{at } A_{\eta\omega} \tag{B.13}$$

$$\nabla\cdot(\mathbf{u}_\omega\mathbf{b}_{\omega\eta}) = \nabla\cdot(\mathbf{D}'_\omega\cdot\nabla\mathbf{b}_{\omega\eta}) - \varphi_\omega^{-1}\mathbf{c}_{\omega\eta} \tag{B.14}$$

$$\mathbf{b}_{\eta\eta}(\mathbf{r}+\ell_i) = \mathbf{b}_{\eta\eta}(\mathbf{r}), \quad i=1,2,3 \tag{B.15}$$

$$\mathbf{b}_{\omega\eta}(\mathbf{r}+\ell_i) = \mathbf{b}_{\omega\eta}(\mathbf{r}), \quad i=1,2,3 \tag{B.16}$$

$$\langle\mathbf{b}_{\eta\eta}\rangle^\eta = 0, \quad \langle\mathbf{b}_{\omega\eta}\rangle^\omega = 0 \tag{B.17}$$

In Eqs. (B.11) and (B.14) two constant vectors have been defined, and they are specified by

$$\mathbf{c}_{\eta\eta} = -\frac{1}{V}\int_{A_{\eta\omega}}\mathbf{n}_{\eta\omega}\cdot(\mathbf{u}_\eta\mathbf{b}_{\eta\eta} - \mathbf{D}'_\eta\cdot\nabla\mathbf{b}_{\eta\eta} - \mathbf{D}'_\eta)\mathrm{d}A \tag{B.18}$$

$$\mathbf{c}_{\omega\eta} = -\frac{1}{V}\int_{A_{\omega\eta}}\mathbf{n}_{\omega\eta}\cdot(\mathbf{u}_\omega\mathbf{b}_{\omega\eta} - \mathbf{D}'_\omega\cdot\nabla\mathbf{b}_{\omega\eta})\mathrm{d}A \tag{B.19}$$

where the two constants are related by

$$\mathbf{c}_{\eta\eta} = -\mathbf{c}_{\omega\eta} \tag{B.20}$$

Problem II. (*Closure problem related to the source* $\nabla\cdot\langle c_\omega\rangle^\omega$)

$$\nabla\cdot(\mathbf{u}_\eta\mathbf{b}_{\eta\omega}) = \nabla\cdot(\mathbf{D}'_\eta\cdot\nabla\mathbf{b}_{\eta\omega}) - \varphi_\eta^{-1}\mathbf{c}_{\eta\omega} \tag{B.21}$$

$$B.C.1 \quad \mathbf{b}_{\eta\omega} = \mathbf{b}_{\omega\omega} \quad at \quad A_{\eta\omega} \tag{B.22}$$

$$B.C.2 \quad \mathbf{n}_{\eta\omega}\cdot(\mathbf{D}'_\eta\cdot\nabla\mathbf{b}_{\eta\omega}) = \mathbf{n}_{\eta\omega}\cdot(\mathbf{D}'_\omega\cdot\nabla\mathbf{b}_{\omega\omega}) + \mathbf{n}_{\eta\omega}\cdot\mathbf{D}'_\omega \quad \text{at } A_{\eta\omega} \tag{B.23}$$

$$\nabla\cdot(\mathbf{u}_\omega\mathbf{b}_{\omega\omega}) + \tilde{\mathbf{u}}_\omega = \nabla\cdot(\mathbf{D}'_\omega\cdot\nabla\mathbf{b}_{\omega\omega}) + \nabla\cdot\mathbf{D}'_\omega - \varphi_\omega^{-1}\mathbf{c}_{\omega\omega} \tag{B.24}$$

$$\mathbf{b}_{\eta\omega}(\mathbf{r}+\ell_i) = \mathbf{b}_{\eta\omega}(\mathbf{r}), \quad i=1,2,3 \tag{B.25}$$

$$\mathbf{b}_{\omega\omega}(\mathbf{r}+\ell_i) = \mathbf{b}_{\omega\omega}(\mathbf{r}), \quad i=1,2,3 \tag{B.26}$$

$$\langle\mathbf{b}_{\eta\omega}\rangle^\eta = 0, \quad \langle\mathbf{b}_{\omega\omega}\rangle^\omega = 0 \tag{B.27}$$

$$\mathbf{c}_{\eta\omega} = -\frac{1}{V}\int_{A_{\eta\omega}}\mathbf{n}_{\eta\omega}\cdot(\mathbf{u}_\eta\mathbf{b}_{\eta\omega} - \mathbf{D}'_\eta\cdot\nabla\mathbf{b}_{\eta\omega})\mathrm{d}A \tag{B.28}$$

$$\mathbf{c}_{\omega\omega} = -\frac{1}{V}\int_{A_{\eta\omega}}\mathbf{n}_{\omega\eta}\cdot(\mathbf{u}_\omega\mathbf{b}_{\omega\omega} - \mathbf{D}'_\omega\cdot\nabla\mathbf{b}_{\omega\omega} - \mathbf{D}'_\omega)\mathrm{d}A \tag{B.29}$$

where the two constants are related by

$$\mathbf{c}_{\eta\omega} = -\mathbf{c}_{\omega\omega} \tag{B.30}$$

Problem III. (*Closure problem related to the exchange source* $\langle c_\omega\rangle^\omega - \langle c_\eta\rangle^\eta$)

$$\nabla\cdot(\mathbf{u}_\eta r_\eta) = \nabla\cdot(\mathbf{D}'_\eta\cdot\nabla r_\eta) - \varphi_\eta^{-1}\alpha^* \tag{B.31}$$

$$B.C.1 \quad r_\eta = r_\omega + 1 \quad \text{at } A_{\eta\omega} \tag{B.32}$$

$$B.C.2 \quad \mathbf{n}_{\eta\omega}\cdot(\mathbf{D}'_\eta\cdot\nabla r_\eta) = \mathbf{n}_{\eta\omega}\cdot(\mathbf{D}'_\omega\cdot\nabla r_\omega) \quad \text{at } A_{\eta\omega} \tag{B.33}$$

$$\nabla\cdot(\mathbf{u}_\omega r_\omega) + \tilde{\mathbf{u}}_\omega = \nabla\cdot(\mathbf{D}'_\omega\cdot\nabla r_\omega) + \varphi_\omega^{-1}\alpha^* \tag{B.34}$$

$$r_\eta(\mathbf{r}+\ell_i) = r_\eta(\mathbf{r}), \quad i=1,2,3 \tag{B.35}$$

$$r_\omega(\mathbf{r}+\ell_i) = r_\omega(\mathbf{r}), \quad i=1,2,3 \tag{B.36}$$

$$\langle r_\eta\rangle^\eta = 0, \quad \langle r_\omega\rangle^\omega = 0 \tag{B.37}$$

$$\alpha^* = -\frac{1}{V}\int_{A_{\eta\omega}}\mathbf{n}_{\eta\omega}\cdot(\varepsilon_\eta\mathbf{v}_\eta r_\eta - \varepsilon_\eta\mathbf{D}_\eta\cdot\nabla r_\eta)\mathrm{d}A = \frac{1}{V}\int_{A_{\omega\eta}}\mathbf{n}_{\omega\eta}\cdot(\varepsilon_\omega\mathbf{v}_\omega r_\omega - \varepsilon_\omega\mathbf{D}_\omega\cdot\nabla r_\omega)\mathrm{d}A \tag{B.38}$$

The closure problems are solved over a representative unit cell. These closure problems assume (1) that periodic boundary conditions are a reasonable condition to impose on the boundaries of the representative unit cell (N.B., this does not imply that the porous medium is actually periodic, but rather is only a convenient device for obtaining a solution; see the discussion in Ref. [86]), and (2) that the characteristic time scale of the deviation concentrations is much smaller than the time scale for diffusion [20]

$$\frac{D'_\eta t^*}{\ell_\eta\varepsilon_\eta} \ll 1, \quad \frac{D'_\omega t^*}{\ell_\omega\varepsilon_\omega} \ll 1 \tag{B.39}$$

The solutions to these closure problems provide the information filtered from the microscale (in terms of the fields $\mathbf{b}_{\eta\eta}$, $\mathbf{b}_{\omega\omega}$, and r_η) that are needed to predict the macroscale effective dispersion tensors and mass transfer coefficient. These effective parameters are given in the body of the paper by Eqs. (47)–(49), and are repeated here

$$\mathbf{D}^*_{\eta\eta} = \langle \mathbf{D}^*_\eta \cdot (\mathbf{I} + \nabla \mathbf{b}_{\eta\eta}) - \tilde{\mathbf{v}}_\eta \mathbf{b}_{\eta\eta} \rangle^\eta \tag{B.40}$$

$$\mathbf{D}^*_{\omega\omega} = \langle \mathbf{D}^*_\omega \cdot (\mathbf{I} + \nabla \mathbf{b}_{\omega\omega}) - \tilde{\mathbf{v}}_\omega \mathbf{b}_{\omega\omega} \rangle^\omega \tag{B.41}$$

$$\begin{aligned} \alpha^* &= -\frac{1}{\mathscr{V}} \int_{A_{\eta\omega}} \mathbf{n}_{\eta\omega} \cdot (\varepsilon_\eta \mathbf{v}_\eta r_\eta - \varepsilon_\eta \mathbf{D}_\eta \cdot \nabla r_\eta) \mathrm{d}A \\ &= \frac{1}{\mathscr{V}} \int_{A_{\omega\eta}} \mathbf{n}_{\omega\eta} \cdot (\varepsilon_\omega \mathbf{v}_\omega r_\omega - \varepsilon_\omega \mathbf{D}_\omega \cdot \nabla r_\omega) \mathrm{d}A \end{aligned} \tag{B.42}$$

The two non-conventional flux terms are given by

$$\begin{aligned} \Omega_\eta = {} & \nabla \cdot [\mathbf{d}_\eta \cdot (\langle c_\eta \rangle^\eta - \langle c_\omega \rangle^\omega)] + \mathbf{u}_{\eta\omega} \cdot \nabla \langle c_\omega \rangle^\omega \\ & + \mathbf{u}_{\eta\eta} \cdot \nabla \langle c_\eta \rangle^\eta + \nabla \cdot [\varphi_\eta \mathbf{D}'_{\eta\omega} \cdot \nabla \langle c_\eta \rangle^\eta] \end{aligned} \tag{B.43}$$

$$\begin{aligned} \Omega_\omega = {} & \nabla \cdot [\mathbf{d}_\omega \cdot (\langle c_\omega \rangle^\omega - \langle c_\eta \rangle^\eta)] + \mathbf{u}_{\omega\omega} \cdot \nabla \langle c_\omega \rangle^\omega \\ & + \mathbf{u}_{\omega\eta} \cdot \nabla \langle c_\eta \rangle^\eta + \nabla \cdot [\varphi_\omega \mathbf{D}'_{\omega\eta} \cdot \nabla \langle c_\eta \rangle^\eta] \end{aligned} \tag{B.44}$$

As mentioned in the body of the paper, the non-conventional flux terms were negligible for this work, and were not considered in further analyses.

Employing these definitions, the upscaled transport equations given by Eqs. (45) and (46) have been closed, and the effective parameters that appear in those transport equations have been formally related to the underlying properties and structure of the Darcy-scale system.

Appendix C. Mass transfer coefficient for a simplified two-region model

This appendix serves two purposes. First, we develop the closure problem for the two-equation model under the conditions that are equivalent to those presented by Rao et al. [78] (see also the development by Glueckauf [29], which has many similarities), and then examine the result if quasi-steady conditions are assumed. Second, we use this as an opportunity to show how closure problems can be expressed in terms of Green's functions, and how this is equivalent to our more standard practice of decomposing the deviations in terms of sources (as done, for example, in Eq. (B.1)).

C.1. A simplified two-region model

For this simplified problem, it is assumed that (1) the heterogeneities are non-interacting spherical inclusions, (2) there is no convection in the inclusions, and (3) that the solute concentration in the matrix is uniform (but possibly time-varying). Under these conditions, Eqs. (27)–(30) take the form

η-region transport equation

$$c_\eta = c_{\eta 0}(t) \quad \text{in the } \eta\text{-region} \tag{C.1}$$

Boundary condition

$$c_\omega = c_{\eta 0}(t) \quad \text{at } A_{\eta\omega} \tag{C.2}$$

ω-region transport equation

$$\varepsilon_\omega \frac{\partial c_\omega}{\partial t} = \nabla \cdot [\varepsilon_\omega D_{\mathrm{eff},\omega} \nabla c_\omega] \quad \text{in the } \omega\text{-region} \tag{C.3}$$

Initial condition

$$c_\eta = 0 \quad \text{at } t = 0 \tag{C.4}$$

$$c_\omega = c_{\omega 0} \quad \text{at } t = 0 \tag{C.5}$$

Following a development identical to the one described in Section 2 of the main body of the paper, the volume averaged transport equations take the form

Macroscale equations

$$\langle c_\eta \rangle^\eta = c_{\eta 0}(t) \quad \text{in the } \eta\text{-region} \tag{C.6}$$

$$c_\omega = c_{\eta 0}(t) \quad \text{at } A_{\eta\omega} \tag{C.7}$$

$$\begin{aligned} \varphi_\omega \varepsilon_\omega \frac{\partial \langle c_\omega \rangle^\omega}{\partial t} = {} & \nabla \cdot [\varphi_\omega \varepsilon_\omega D_{\mathrm{eff},\omega} \nabla \langle c_\omega \rangle^\omega] \\ & + \frac{1}{V} \int_{A_{\eta\omega}} \mathbf{n}_{\omega\eta} \cdot (\varepsilon_\omega D_{\mathrm{eff},\omega} \nabla \tilde{c}_\omega) \mathrm{d}A \end{aligned} \tag{C.8}$$

Initial condition

$$c_\eta = 0 \quad \text{at } t = 0 \tag{C.9}$$

$$c_\omega = c_{\omega 0} \quad \text{at } t = 0 \tag{C.10}$$

The η-phase concentration can be found by conducting a total mass balance on the two phases. Any mass 'lost' by the inclusions is gained by the matrix, allowing one to express the concentration $c_\eta(t)$ by

$$c_{\eta 0}(t) = \frac{\varphi_\omega (c_{\omega 0} - \langle c_\omega \rangle^\omega)}{\varphi_\eta} \quad \text{at } t \geqslant 0 \tag{C.11}$$

An additional term arises in the averaging process, but it is identically zero for the cylindrical or spherical geometry assumed for this development, i.e.,

$$\frac{1}{\mathscr{V}} \int_{A_{\eta\omega}} \mathbf{n}_{\eta\omega} \tilde{c}_\omega \, \mathrm{d}A = 0 \tag{C.12}$$

This set of equations leads to a quasi-steady closure problem that takes the form

Closure problem:

$$\varepsilon_\omega \frac{\partial \tilde{c}_\omega}{\partial t} = \varepsilon_\omega D_{eff,\omega} \nabla^2 \tilde{c}_\omega - \underbrace{\varphi_\omega^{-1} \alpha^*(t) C_{\eta\omega}(t)}_{\text{Source Term}} \quad \text{in the } \omega\text{-region} \tag{C.13}$$

$$\tilde{c}_\omega = \underbrace{C_{\eta\omega}(t)}_{\text{Source Term}} \quad \text{at } A_{\eta\omega} \tag{C.14}$$

$$\tilde{c}_\omega = 0 \quad \text{at } t = 0 \tag{C.15}$$

where $C_{\eta\omega}(t)$ represents the difference in the macroscale concentration

$$C_{\eta\omega}(t) = c_{\eta 0}(t) - \langle c_\omega \rangle^\omega \quad \text{at } A_{\eta\omega} \tag{C.16}$$

and $\alpha^*(t)$ is a function of only time, given by

$$\alpha^*(t) = C_{\eta\omega}^{-1}\frac{1}{V}\int_{A_{\eta\omega}} \mathbf{n}_{\omega\eta}\cdot(\varepsilon_\omega D_{\mathrm{eff},\omega}\nabla\tilde{c}_\omega)\mathrm{d}A \tag{C.17}$$

We need to point out here that the appearance of $C_{\eta\omega}(t)$ in the source term in Eq. (C.13) is artificial, but convenient.

This set of equations has two time-varying sources, the heterogeneous source $\varphi_\omega^{-1}\alpha^*(t)C_{\eta\omega}(t)$, and the boundary source $C_{\eta\omega}(t)$. Under the constraints that have been imposed already (i.e., Eq. (50)), both quantities can be considered to be spatially constant for the purposes of the closure problem. However, because they are both explicit functions of time, they cannot, in general, be considered to be time independent. One might hope to find conditions for which the following restriction is valid

$$\varepsilon_\omega\frac{\partial\tilde{c}_\omega}{\partial t} \ll \varepsilon_\omega D_{\mathrm{eff},\omega}\nabla^2\tilde{c}_\omega \tag{C.18}$$

which would allow the closure problem to be treated as *quasi-steady*. However, because the inclusions are assumed to be diffusion-dominated, it is difficult to envision conditions where the concentration deviations and the average concentration have dramatically different time scales.

There are essentially two ways to proceed from here: (1) maintain the explicit coupling between the macroscale and microscale equations, and solve a *transient* closure problem to determine a time-dependent mass transfer coefficient, $\alpha^*(t)$; or (2) adopt the simplification given by Eq. (C.18) that allows one to determine a non-time-dependent mass transfer coefficient. The subsequent task for this latter approach would be to assign a definite meaning to this (constant) value for α^*, and to determine how this assumption influences the representation of the mass transfer process.

The first approach was the method adopted by Rao et al. [78] for the mobile/immobile model for spherical inclusions, and it has begun to be explored in the context of volume averaging theory [42,85]. Although explicit analytical solutions can be obtained for the simples cases (e.g. where the inclusions have no convection, the geometry is ideal, and there is a separation of time scales for transport in the two regions) in general this approach yields complex integro-differential equations which can be very complicated to solve. As an alternative, we have pursued option (2) here. Some additional comments regarding this approach are provided below.

Before proceeding further, we make the substitution $\tilde{c}_\omega^0 = \tilde{c}_\omega/C_{\eta\omega}$. The quasi-steady closure problem takes the form

Quasi-steady closure problem

$$\nabla^2\tilde{c}_\omega^0 = \frac{\alpha^*}{\varphi_\omega\varepsilon_\omega D_{\mathrm{eff},\omega}} \quad \text{in the } \omega\text{-region} \tag{C.19}$$

$$\tilde{c}_\omega^0 = 1 \quad \text{at } A_{\eta\omega} \tag{C.20}$$

where now both α^* and $C_{\eta\omega}$ are treated as being true constants (time and space-independent) for the purposes of the closure problem. This treatment imposes some interesting constraints on the resulting value of α^*, and these will be discussed in further detail below. The closure problem now takes the form that has simple solution in terms of Green's functions

$$\tilde{c}_\omega = \frac{C_{\eta\omega}\alpha^*}{\varphi_\omega\varepsilon_\omega D_{\mathrm{eff},\omega}}\int_{V_\omega(\mathbf{x}')} G(\mathbf{x};\mathbf{x}')\mathrm{d}V(\mathbf{x}') + C_{\eta\omega}\int_{A_{\eta\omega}(\mathbf{x}')}\mathbf{n}_{\omega\eta}\cdot\nabla_{\mathbf{x}'}G(\mathbf{x};\mathbf{x}')\mathrm{d}A(\mathbf{x}') \tag{C.21}$$

where G is the Green's function associated with the Dirichlet problem given by Eqs. (C.19) and (C.20). Note that this solution takes the form analogous to that of Eq. (B.2):

$$\tilde{c}_\omega = r_\omega(\langle c_\omega\rangle^\omega - \langle c_\eta\rangle^\eta) \tag{C.22}$$

where

$$r_\omega = \frac{\alpha^*}{\varphi_\omega\varepsilon_\omega D_{eff,\omega}}\int_{V_\omega(\mathbf{x}')} G(\mathbf{x};\mathbf{x}')\mathrm{d}V(\mathbf{x}') + \int_{A_{\eta\omega}(\mathbf{x}')}\mathbf{n}_{\omega\eta}\cdot\nabla_{\mathbf{x}'}G(\mathbf{x};\mathbf{x}')\mathrm{d}A(\mathbf{x}') \tag{C.23}$$

This result establishes the correspondence between the Green's function solution to the closure problem and the conventional closure variables that are usually used in the method of volume averaging (e.g. Eqs. (B.1) and (B.2)).

For the closure of Eq. (C.8), we need the quantity $\nabla\tilde{c}_\omega$, which is given by

$$\nabla\tilde{c}_\omega = \frac{C_{\eta\omega}\alpha^*}{\varphi_\omega\varepsilon_\omega D_{\mathrm{eff},\omega}}\int_{V_\omega(\mathbf{x}')}\nabla G(\mathbf{x};\mathbf{x}')\mathrm{d}V(\mathbf{x}') + C_{\eta\omega}\nabla\int_{A_{\eta\omega}(\mathbf{x}')}\mathbf{n}_{\omega\eta}\cdot\nabla_{\mathbf{x}'}G(\mathbf{x};\mathbf{x}')\mathrm{d}A(\mathbf{x}') \tag{C.24}$$

Using the properties of Green's functions, it is easy to show

$$\int_{A_{\eta\omega}(\mathbf{x}')}\mathbf{n}_{\omega\eta}\cdot\nabla_{\mathbf{x}'}G(\mathbf{x};\mathbf{x}')\mathrm{d}A(\mathbf{x}') = 1 \tag{C.25}$$

hence, the second term on the right-hand side of Eq. (C.24) is zero, and the notation $A_{\eta\omega}(\mathbf{x}')$ indicates integration over the set of points on the surface $A_{\eta\omega}$. Rearranging what remains from Eq. (C.24) we have

$$\varepsilon_\omega D_{eff,\omega}\nabla\tilde{c}_\omega = \frac{VC_{\eta\omega}\alpha^*}{V_\omega}\int_{V_\omega(\mathbf{x}')}\nabla G(\mathbf{x};\mathbf{x}')\mathrm{d}V(\mathbf{x}') \tag{C.26}$$

where we have used the definition $\varphi_\omega = V_\omega/V$, and the notation $V_\omega(\mathbf{x}')$ indicates integration over the set of points in the volume V_ω. Substituting this result into the unclosed macroscale equation give by Eq. (C.8) and interchanging the order of integration gives

$$\varphi_\omega\varepsilon_\omega\frac{\partial\langle c_\omega\rangle^\omega}{\partial t} = \nabla\cdot[\varphi_\omega\varepsilon_\omega D_{eff,\omega}\nabla\langle c_\omega\rangle^\omega] + \frac{C_{\eta\omega}\alpha^*}{V_\omega}\int_{V_\omega(\mathbf{x}')}\int_{A_{\eta\omega}}\mathbf{n}_{\omega\eta}\cdot\nabla G(\mathbf{x};\mathbf{x}')\mathrm{d}A\,\mathrm{d}V(\mathbf{x}') \tag{C.27}$$

Finally, once again noting the identity given by Eq. (C.25), we find the result

$$\varepsilon_\omega \varphi_\omega \frac{\partial \langle c_\omega \rangle^\omega}{\partial t} = \nabla \cdot [\varepsilon_\omega \varphi_\omega D_{\text{eff},\omega} \nabla \langle c_\omega \rangle^\omega] - \alpha^* (c_{\eta 0} - \langle c_\omega \rangle^\omega) \tag{C.28}$$

Note that conventionally the macroscale diffusion term is dropped relative to the interfacial mass transfer term yielding the expression (cf. Cherblanc et al. [40], Eq. (77))

$$\varepsilon_\omega \varphi_\omega \frac{\partial \langle c_\omega \rangle^\omega}{\partial t} = \alpha^* (c_{\eta 0} - \langle c_\omega \rangle^\omega) \tag{C.29}$$

C.2. Interpretation of the effective mass transfer coefficient

Although this establishes a steady-state solution for predicting α^*, it is not clear from this solution exactly how α^* relates to a more general, transient closure scheme. To answer this question, it is convenient to expand the deviation concentration in terms of eigenfunctions. The steady closure problem is a linear problem that is identical to the Dirichlet problem on a sphere. In this case, the right-hand side of Eq. (C.19) is a constant, but an unknown one. A set of orthonormal eigenfunctions for this problem exists, and we will denote these functions by $w_{mn}(\mathbf{x})$. One can expand the Green's function for this problem in terms of these eigenfunctions (cf. Ref. [87], Section 10.7), yielding the following expression for $\tilde{c}_\omega$

$$\tilde{c}_\omega(\mathbf{x}) = -\frac{C_{\eta\omega}\alpha^*}{\varphi_\omega \varepsilon_\omega D_{\text{eff},\omega}} \int_{V_\omega(\mathbf{x}')} \sum_{m=1}^{\infty} \sum_{n=1}^{\infty} \times \frac{1}{\lambda_{mn}} w_{mn}(\mathbf{x}) w_{mn}(\mathbf{x}') \mathrm{d}V(\mathbf{x}') + C_{\eta\omega} \tag{C.30}$$

For this expression, integration and summation can be interchanged, yielding

$$\tilde{c}_\omega(\mathbf{x}) = -\frac{C_{\eta\omega}\alpha^*}{\varphi_\omega \varepsilon_\omega D_{\text{eff},\omega}} \sum_{m=1}^{\infty} \sum_{n=1}^{\infty} \frac{V_\omega}{\lambda_{mn}} w_{mn}(\mathbf{x}) \langle w_{mn} \rangle^\omega + C_{\eta\omega} \tag{C.31}$$

This expression still has one unknown constant, α^*. We can determine α^* if we have an additional independent equation. For the steady closure, we can impose the condition $\langle \tilde{c}_\omega \rangle^\omega = 0$. Imposing this constraint, we can take the average of both sides of Eq. (C.31) to yield

$$\frac{\alpha^*}{\varphi_\omega \varepsilon_\omega D_{\text{eff},\omega}} \sum_{m=1}^{\infty} \sum_{n=1}^{\infty} \frac{V_\omega (\langle w_{mn} \rangle^\omega)^2}{\lambda_{mn}} = 1 \tag{C.32}$$

As a direct result of Parseval's equality [88] for a weighting function equal to $1/V_\omega$, we must have the condition that

$$\sum_{m=1}^{\infty} \sum_{n=1}^{\infty} V_\omega (\langle w_{mn} \rangle^\omega)^2 = 1 \tag{C.33}$$

From this expression, it is clear that the terms $V_\omega (\langle w_{mn} \rangle^\omega)^2$ can be considered to be weights for each of the eigenvalues, λ_{mn}. We find that α^* is proportional to the harmonic average of the eigenvalues of the closure problem

$$\alpha^* = \varepsilon_\omega D_{\text{eff},\omega} \varphi_\omega^{-1} \left(\sum_{m=1}^{\infty} \sum_{n=1}^{\infty} \frac{V_\omega (\langle w_{mn} \rangle^\omega)^2}{\lambda_{mn}} \right)^{-1} \tag{C.34}$$

To complete this definition, we note that we can assign a definite value to α^* for the particular problem discussed in this appendix. The solution to (C.19) and (C.20) is straightforward [89], and $\tilde{c}_\omega$ is given by

$$\tilde{c}_\omega(\mathbf{x}) - C_{\eta\omega} = -\frac{C_{\eta\omega}\alpha^*}{\varphi_\omega \varepsilon_\omega D_{\text{eff},\omega}} (a^2 - \mathbf{x} \cdot \mathbf{x}) \tag{C.35}$$

where a is the radius of the sphere. Averaging both sides of this equation, and noting the condition imposed earlier ($\langle \tilde{c}_\omega \rangle^\omega = 0$) one obtains the relation

$$1 = \frac{\alpha^*}{\varphi_\omega \varepsilon_\omega D_{\text{eff},\omega}} (a^2 - \langle \mathbf{x} \cdot \mathbf{x} \rangle^\omega) \tag{C.36}$$

The value of $\langle \mathbf{x} \cdot \mathbf{x} \rangle^\omega$ is determined by a simple integration to provide

$$\langle \mathbf{x} \cdot \mathbf{x} \rangle^\omega = \frac{3}{5} a^2 \tag{C.37}$$

Substituting this into Eq. (C.36) one finds that for the simple unit cell consisting of a periodic array of spheres, the value of α^* is found to be

$$\alpha^* = \frac{15}{a^2} \varphi_\omega \varepsilon_\omega D_{\text{eff},\omega} \tag{C.38}$$

Noting that many references define the effective diffusion coefficient in porous media by

$$D'_{\text{eff},\omega} = \varepsilon_\omega D_{\text{eff},\omega} \tag{C.39}$$

we find that Eq. (C.38) represents the harmonic average of the eigenvalues of the Laplace operator for our particular boundary value problem, and that this value is consistent with the value proposed previously for α^* [29,30,35]. A similar analysis for cylindrical inclusions [42] leads to the value $\alpha^* = 8\varphi_\omega \varepsilon_\omega D_{\text{eff},\omega}/a^2$. Further discussion about the derivation of steady values for α^* from the perspective of volume averaging are presented by Cherblanc et al. (Ref. [40], Section 5.1).

It is interesting to note that the steady solution of the closure problem specifies a value for α^* that is generally different from the asymptotic and time-averaged values of α^* developed by Rao et al. [78] (where for that work, the leading coefficient is a value between about 10 and 20, depending upon the value of φ_ω). The only difference between the approach developed above and that of Rao et al. [78] is that in this work the source term $C_{\eta\omega}$ (representing the difference between the average concentrations in the two regions) is treated as a constant. We can only conclude that by forcing a decoupling between the micro- and macroscale equations (i.e., by treating $C_{\eta\omega}$ as a constant) we force the system of equations to predict the harmonic average value of α^*. Because it has been shown previously by Harvey and Gorelick [30] that this value for α^* forces the zeroth, first, and second temporal moments of the breakthrough curve to be maintained, we can consider prediction

of α^* from the steady closure problem to be optimal in this sense.

References

[1] Berkowitz B, Scher H, Silliman SE. Anomalous transport in laboratory-scale, heterogeneous porous media. Water Resour Res 2000;36:149–58.

[2] Benson DA, Wheatcraft SW, Meerschaert MM. Application of a fractional advection–dispersion equation. Water Resour Res 2000;36:1403–12.

[3] Haggerty R, McKenna SA, Meigs LC. On the late-time behavior of tracer breakthrough curves. Water Resour Res 2000;36:3467–79.

[4] Meerschaert MM, Benson DA, Bäumer B. Multidimensional advection and fractional dispersion. Phys Rev E 1999;59:5026–8.

[5] Margolin G, Berkowitz B. Application of continuous time random walks to transport in porous media. J Phys Chem B 2000;104:3942–7.

[6] Schumer R, Benson DA, Meerschaert MM, Baeumer B. Fractal mobile/immobile solute transport. Water Resour Res 2003;39:1296. doi:10.1029/2003WR003141.

[7] Cushman JH, Ginn TR. Fractional advection-dispersion equation: a classical mass balance with convolution-Fickian flux. Water Resour Res 2000;36:3763–6.

[8] Deng F-W, Cushman JH. Comparison of moments for classical-, quasi-, and convolution-Fickian dispersion of a conservative tracer. Water Resour Res 1995;31:1147–9.

[9] Wood BD, Kavvas ML. Correction to "Stochastic solute transport under unsteady flow conditions: comparison of theory, Monte Carlo simulations, and field data" by Brian D. Wood and M. Levent Kavvas. Water Resour Res 1999;35:2889.

[10] Wood BD, Kavvas ML. Stochastic solute transport under unsteady flow conditions: comparison of theory, Monte Carlo simulations, and field data. Water Resour Res 1999;35:2889.

[11] Wood BD, Kavvas ML. Correction to "Ensemble-averaged equations for reactive transport in porous media under unsteady flow conditions" by Brian D. Wood and M. Levent Kavvas. Water Resour Res 1999;35:2887.

[12] Wood BD, Kavvas ML. Ensemble-averaged equations for reactive transport in porous media under unsteady flow conditions. Water Resour Res 1999;35:2887.

[13] Wood BD. A connection between the Lagrangian stochastic-convective and cumulant expansion approaches for describing solute transport in heterogeneous porous media. Adv Water Resour 1998;22:319–32.

[14] Simmons CS, Kincaid CT. Scale-dependent effective dispersion coefficients for one-dimensional solute transport. Proceedings of the seventh annual AGU front range branch hydrology days, 21–23 April, 1987. Fort Collins: Colorado State University; 1987.

[15] Zhang Q. The asymptotic scaling behavior of mixing induced by random velocity field. Adv Appl Math 1995;16:23–58.

[16] Zhang Q. Multi-length-scale theories for scale-up problem and renormalized perturbation expansion. Adv Water Resour 1997;20:317–33.

[17] Panfilov M. Macroscale models of flow through highly heterogeneous porous media. Dordrecht: Kluwer; 2000.

[18] Auriault JL, Lewandowska J. Non-Gaussian diffusion modeling in composite porous-media by homogenization – tail effect. Transp Porous Med 1995;21:47–70.

[19] Quintard M, Cherblanc F, Whitaker S. Dispersion in heterogeneous porous media: one-equation non-equilibrium model. Transp Porous Med 2001;44:181–203.

[20] Ahmadi A, Quintard M, Whitaker S. Transport in chemically and mechanically heterogeneous porous media, V., two-equation model for solute transport with adsorption. Adv Water Resour 1998;22:59–86.

[21] Dagan G, Fiori A, Jankovic I. Flow and transport in highly heterogeneous formations: 1. Conceptual framework and validity of first-order approximations. Water Resour Res 2003;39:1268.

[22] Haggerty R, Gorelick SM. Multiple-rate mass transfer for modeling diffusion and surface reactions in media with pore-scale heterogeneity. Water Resour Res 1995;31:2383–400.

[23] Jankovic I, Fiori A, Dagan G. Flow and transport through two-dimensional isotropic media of binary conductivity distribution. Part 2: NUMERICAL simulations and comparison with theoretical results. Stoch Environ Res Risk Assess 2003;17:384–93.

[24] Jankovic I, Fiori A, Dagan G. Flow and transport in highly heterogeneous formations: 3. Numerical simulations and comparison with theoretical results. Water Resour Res 2003;39:1270.

[25] Brown CJ, Coates JD, Schoonen MAA. Localized sulfate-reducing zones in a coastal plain aquifer. Ground Water 1999;37:505–16.

[26] Murphy EM, Schramke JA, Fredrickson JK, Bledsoe HW, Francis AJ, Sklarew DS et al. The influence of microbial activity and sedimentary organic carbon on the isotope geochemistry of the Middendorf aquifer. Water Resour Res 1992;28:723–40.

[27] de Smedt F, Wierenga PJ. Mass transfer in porous media with immobile water. J Hydrol 1979;41:59–67.

[28] Parker JC, Valocchi AJ. Constraints on the validity of equilibrium and first-order kinetic transport models in structured soils. Water Resour Res 1986;22:399–407.

[29] Glueckauf E. Theory of chromatography, part 10, Formulae for diffusion into spheres and their application to chromatography. Trans Faraday Soc 1955;51:1540–51.

[30] Harvey CF, Gorelick SM. Temporal moment-generating equations: modeling transport and mass transfer in heterogeneous aquifers. Water Resour Res 1995;31:1895–911.

[31] Nkedi-Kizza P et al. On the equivalence of two conceptual models for describing ion exchange during transport through an aggregated oxisol. Water Resour Res 1984;20:1123–30.

[32] Young DF, Ball WP. Estimating diffusion coefficients in low-permeability porous media using a macropore column. Environ Sci Technol 1998;32:2578–84.

[33] Rabideau AJ, Miller CT. Two-dimensional modeling of aquifer remediation influenced by sorption nonequilibrium and hydraulic conductivity heterogeneity. Water Resour Res 1994;30:1457–70.

[34] Raats PAC. Transport in structured porous media. Proc Euromech 1981;143:221–6.

[35] Raats PAC. Tracing parcels of water and solutes in unsaturated zones. In: Yaron B, Dagan G, editors. Pollutants in porous media: the unsaturated zone between soil surface and groundwater. New York: Springer-Verlag; 1984.

[36] Griffioen J. Suitability of the first-order mass transfer concept for describing cyclic diffusive mass transfer in stagnant zones. J Contam Hydrol 1998;34:155–65.

[37] Cunningham JA, Roberts PV. Use of temporal moments to investigate the effects of nonuniform grain-size distribution on the transport of sorbing solutes. Water Resour Res 1998;34:1415–25.

[38] Carrera J et al. Solution methods and qualitative effects. Hydrogeol J 1998;6:178–90.

[39] Bertin H, Panfilov M, Quintard M. Two types of transient phenomena and full relaxation macroscale model for single phase flow through double porosity media. Transp Porous Med 2000;39:73–96.

[40] Cherblanc F, Ahmadi A, Quintard M. Two-medium description of dispersion in heterogeneous porous media: calculation of macroscopic properties. Water Resour Res 2003;39:1154. doi:10.1029/2002WR001559.

[41] Cherblanc F, Ahmadi A, Quintard M. Two-domain description of solute transport in heterogeneous porous media: Comparison between theoretical predictions and numerical experiments. Adv Water Resour 2007;30:1127–43.

[42] Moyne C. Two-equation model for a diffusive process in porous media using the volume averaging method with an unsteady state closure. Adv Water Resour 1996;20:63–76.

[43] Chastanet J, Wood BD. The mass transfer process in a two-region medium. Water Resour Res, in review.

[44] Zinn B, Meigs LC, Harvey CF, Haggerty R, Peplinski WJ, von Schwerin CF. Experimental visualization of solute transport and

mass transfer processes in two-dimensional conductivity fields with connected regions of high conductivity. Environ Sci Technol 2004;38:3916–26.
[45] Dykhuizen RC. A new coupling term for dual-porosity models. Water Resour Res 1990;26:351–6.
[46] Gerke HH, Van Genuchten MT. A dual-porosity model for simulating the preferential movement of water and solutes in structured porous media. Water Resour Res 1993;29:305–19.
[47] Gerke HH, Van Genuchten MT. Macroscopic representation of structural geometry for simulating water and solute movement in dual-porosity media. Adv Water Resour 1996;19:343–57.
[48] Gwo J, Jardine P, Wilson G, Yeh G. Using a multiregion model to study the effects of advective and diffusive mass transfer on local physical non-equilibrium and solute mobility in a structured soil. Water Resour Res 1996;32:561–70.
[49] Skopp J, Gardner WR, Tyler EJ. Solute movement in structured soils: two-region model with small interaction. Soil Sci Am J 1981;45: 837–42.
[50] Vogel T, Gerke H, Zhang R, Genuchten MV. Modelling flow and transport in a two-dimensional dual-permeability system with spatially variable hydraulic properties. J Hydrol 2000;238:78–89.
[51] Barenblatt GE, Sheltov IP, Kochina IN. Basic concept of the theory of seepage of homogeneous liquids in fissured rocks. J Appl Math Mech 1960;24:1286–303.
[52] Goltz MN, Roberts PV. Three-dimensional solutions for solute transport in an infinite medium with mobile and immobile zones. Water Resour Res 1986;22:1139–48.
[53] van Genuchten MT, Wierenga PJ. Mass transfer studies in sorbing porous media: I. Analytical solutions. Soil Sci Am J 1976;40:473–80.
[54] Zurmühl T, Durner W. Modeling transient water and solute transport in a biporous soil. Water Resour Res 1996;32:819–29.
[55] Quintard M, Whitaker S. Transport in chemically and mechanically heterogeneous porous media IV: large-scale mass equilibrium for solute transport with adsorption. Adv Water Resour 1998;22:59–86.
[56] Whitaker S. The method of volume averaging. In: Bear J, editor. Theory and applications of transport in porous media. Dordrecht: Kluwer; 1999.
[57] Bear J. Hydraulics of groundwater. In: Chow VT, Linsley RK, editors. McGraw-Hill Series inf Water Resources and Environmental Engineering. New York: McGraw-Hill; 1979. p. 569.
[58] Takacs L. A two-step scheme for the advection equation with minimised dissipation and dispersion errors. Mon Weather Rev 1985;113:1050–65.
[59] Bruneau CH, Fabrie P, Rasetarinera P. An accurate finite difference scheme for solving convection-dominated diffusion equations. Int J Numer Meth Fluids 1997;24:169–83.
[60] Edwards MG, Rogers CF. Finite volume discretization with imposed flux continuity for the general tensor pressure equation. Comput Geosci 1998;2:259–90.
[61] Bear J. On the tensor form of dispersion in porous media. J Geophys Res 1961;66:1185–97.
[62] Flury M, Wai NN. Dyes as tracers for vadose zone hydrology. Rev Geophys 2003;41:1002. doi:10.1029/2001RG000109.
[63] Gray WG et al. Mathematical tools for changing spatial scales in the analysis of physical systems. Boca Raton, FL: CRC Press; 1993.
[64] Anderson TB, Jackson R. A fluid mechanical description of fluidized beds. Ind Eng Chem Fundam 1967;6:527–38.
[65] Cushman JH. Volume averaging, probabilistic averaging, and ergodicity. Adv Water Res 1983;6:182–4.
[66] Howes FA, Whitaker S. The spatial averaging theorem revisited. Chem Eng Sci 1985;40:1387–92.
[67] Slattery JC. Flow of viscoelastic fluids through porous media. AIChE J 1967;13:1066–71.
[68] Whitaker S. Diffusion and dispersion in porous media. AIChE J 1967;13:420–7.
[69] Gwo J-P, O'Brien R, Jardine P. Mass transfer in structured porous media: embedding mesoscale structure and microscale hydrodynamics in a two-region model. J Hydrol 1998;208:204–22.
[70] Kitanidis PK. The concept of the dilution index. Water Resour Res 1994;30:2011–26.
[71] van Genuchten MT, Dalton FN. Models for simulating salt movement in aggregated field soils. Geoderma 1986;38:165–83.
[72] Landerau P, Noetinger B, Quintard M. Quasi-steady two-equation models for diffusive transport in fractured porous media: large-scale properties for densely fractured systems. Adv Water Resour 2001;24: 863–76.
[73] Chen Z-X. Transient flow of slightly compressible fluids through double-porosity, double-permeability systems – a state-of-the-art review. Transport Porous Med 1989;4:147–84.
[74] Rao PSC et al. Solute transport in aggregated porous media: theoretical and experimental evaluation. Soil Sci Am J 1980;44: 1139–46.
[75] Bibby R. Mass transport of solutes in dual-porosity media. Water Resour Res 1981;17:1075–81.
[76] Pruess K, Narasimhan TN. A practical method for modeling fluid and heat flow in fractured porous media. Soc Petrol Eng J 1985;25: 14–26.
[77] Gilman JR. An efficient finite-difference method for simulating phase segregation in the matrix blocks in double-porosity reservoirs. SPE Reservoir Eng 1996:403–13.
[78] Rao PSC, Rolston D, Jessup R, Davidson J. Experimental and mathematical description of nonadsorbed solute transfer by diffusion in spherical aggregates. Soil Sci Am J 1980;44:684–8.
[79] Kfoury M, Ababou R, Nœtinger B, Quintard M. Matrix-fracture exchange in a fractured porous medium: stochastic upscaling. Comptes Rendus Mec 2004;332:679–86.
[80] Rayleigh LJWS. On the influence of obstacles arranged in rectangular order upon the properties of the medium. Philos Mag 1892;34:481–9.
[81] Quintard M. Diffusion in isotropic and anisotropic porous systems. Transport Porous Med 1993;11:187–99.
[82] Quintard M, Kaviany M, Whitaker S. Two-medium treatment of heat transfer in porous media: numerical results for effective properties. Adv Water Resour 1997;20:77–94.
[83] Shonnard DR, Whitaker S. The effective thermal conductivity for a point-contact porous medium: an experimental study. Int J Heat Mass Transfer 1989;37:2817–34.
[84] Fabrie P, Quintard M, Whitaker S. Calculation of porous media effective properties: computational problems and required unit cell features. Proceedings of the conference on mathematical modelling of flow through porous media. London: World Scientific Publishing Company; 1995.
[85] Landerau P. Modèles macroscopiques pour les écoulements monophasiques en milieux poreux fracturés: application au tests de puits. pH.D. thesis, University of Bordeaux I, 2000.
[86] Wood BD et al. Volume averaging for determining the effective dispersion tensor: closure using periodic unit cells and comparison with ensemble averaging. Water Resour Res 2003;38(8):1210. doi:10.1029/2002WR001723.
[87] Myint-U T, Debnath L. Partial differential equations for scientists and engineers. 3rd ed. Englewood Cliffs (NJ): Prentice-Hall; 1987.
[88] Coddington EA, Levinson N. Theory of ordinary differential equations. New York: McGraw-Hill; 1955.
[89] Carslaw HS, Jaeger JC. Conduction of heat in solids. 2nd ed. Oxford: Oxford University (Clarendon) Press; 1959.